3D-aware Blending with Generative NeRFs

Hyunsu Kim [1]   Gayoung Lee [1]   Yunjey Choi [1]   Jin-Hwa Kim [1,2]   Jun-Yan Zhu[3]

[1]NAVER AI Lab   [2]SNU AIIS   [3]CMU

Abstract

Image blending aims to combine multiple images seamlessly. It remains challenging for existing 2D-based methods, especially when input images are misaligned due to differences in 3D camera poses and object shapes. To tackle these issues, we propose a 3D-aware blending method using generative Neural Radiance Fields (NeRF), including two key components: 3D-aware alignment and 3D-aware blending. For 3D-aware alignment, we first estimate the camera pose of the reference image with respect to generative NeRFs and then perform 3D local alignment for each part. To further leverage 3D information of the generative NeRF, we propose 3D-aware blending that directly blends images on the NeRF's latent representation space, rather than raw pixel space. Collectively, our method outperforms existing 2D baselines, as validated by extensive quantitative and qualitative evaluations with FFHQ and AFHQ-Cat.

1. Introduction

Image blending aims at combining elements from multiple images naturally, enabling a wide range of applications in content creation, and virtual and augmented realities [105, 106]. However, blending images seamlessly requires delicate adjustment of color, texture, and shape, often requiring users' expertise and tedious manual processes. To reduce human efforts, researchers have proposed various automatic image blending algorithms, including classic methods [9, 55, 70, 84] and deep neural networks [61, 88, 102].

Despite significant progress, blending two unaligned images remains a challenge. Current 2D-based methods often assume that object shapes and camera poses have been accurately aligned. As shown in Figure 1, even slight misalignment can produce unnatural results, as it is obvious to human eyes that foreground and background objects were captured using different cameras. Several methods [14, 36, 58, 75, 94] warp an image via 2D affine transformation. However, these approaches do not account for 3D geometric differences, such as out-of-plane rotation and 3D shape differences. 3D alignment is much more difficult for users and algorithms, as it requires inferring the 3D structure from a single view.
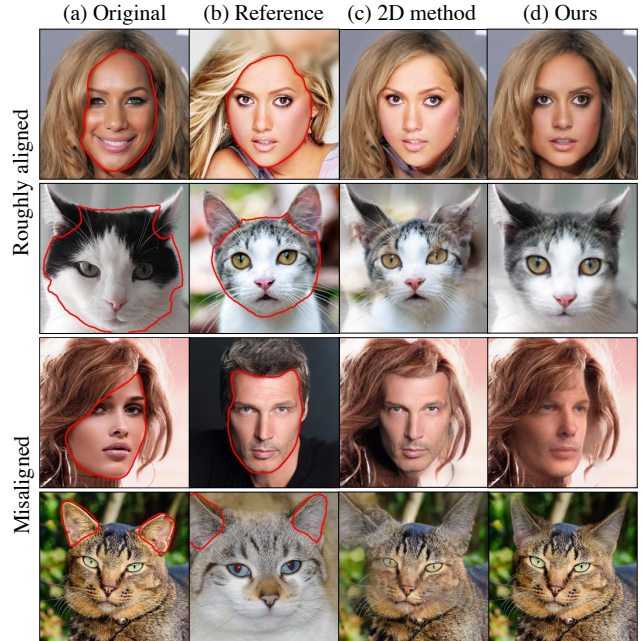

Figure 1. Image blending is challenging for unaligned original and reference images. Existing 2D-based methods [47] struggle to synthesize realistic results due to the 3D object pose differences between foreground and background. In contrast, we propose a 3D-aware blending method that aligns and composes unaligned images without manual effort.

To address the above issues, we propose a 3D-aware image blending method based on generative Neural Radiance Fields (NeRFs) [11, 12, 34, 67, 76, 100]. Generative NeRFs learn to synthesize images in 3D using only collections of single-view images. Our method projects the input images to the volume density representation of generative NeRFs. We then perform 3D-aware blending on these NeRFs' latent representation spaces. Concretely, we formulate an optimization problem in which a latent code is optimized to synthesize the foreground close to the reference images while preserving the background of the original image.

Figure 2 shows critical differences between our approach and previous methods. Figure 2a shows a classic 2D blending method composing two 2D images without alignment. We then show the performance of the 2D blending method can
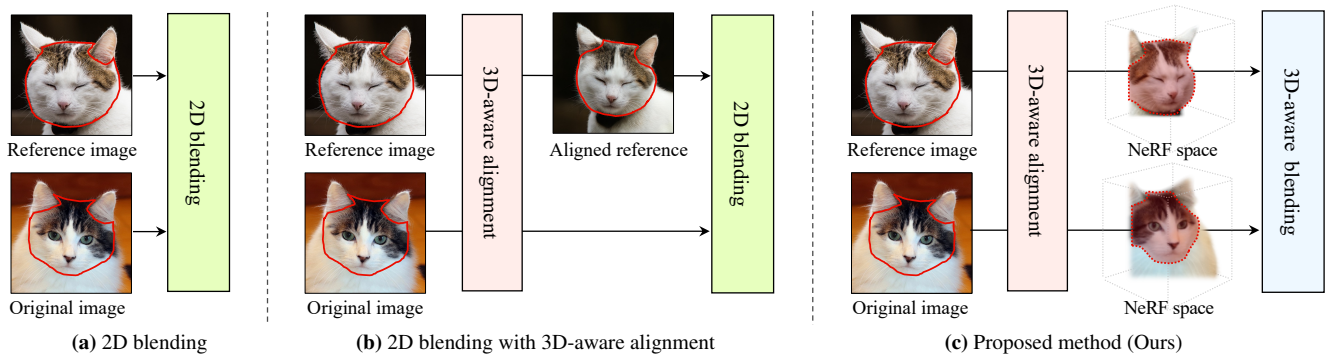
(a) 2D blending   **(b)** 2D blending with 3D-aware alignment   **(c)** Proposed method (Ours)

Figure 2. **Comparison with the existing blending methods.** Red lines denote target blending parts. **(a) 2D blending.** 2D blending methods compose two images without any 3D-aware alignment. **(b) 2D blending with 3D-aware alignment.** To address misalignment, we apply our 3D-aware alignment method to existing 2D blending methods. **(c) Proposed method.** We propose 3D-aware blending after applying our 3D-aware alignment. Note that all methods do not use 3D labels or 3D morphable models.

be improved using our 3D-aware alignment with generative NeRFs as shown in Figure 2b. To further exploit 3D information, we propose to compose two images in NeRFs' latent representation spaces instead of 2D pixel space. Figure 2c shows our final method.

We demonstrate the effectiveness of our method on unaligned images with different poses and scales (*e.g.*, Figure 1). Extensive experiments show that our method outperforms both classic and learning-based methods regarding both photorealism and faithfulness to the input images. Additionally, our method can disentangle color and geometric changes during blending, and create view-consistent results. To our knowledge, our method is the first general-purpose 3D-aware image blending method capable of blending a diverse set of unaligned images. Please find the code and data on our project page.

2. Related Work

Image blending aims to compose different visual elements into a single image. Seminal works tackle this problem using various low-level visual cues, such as image gradients [29, 40, 70, 82, 83], frequency bands [8, 9], color and noise transfer [80, 89], and segmentation [1, 55, 57, 73]. Later, researchers developed data-driven systems to compose objects with similar lighting conditions, camera poses, and scene contexts [17, 36, 56].

More recently, various learning-based methods have been proposed, including blending deep features instead of pixels [22, 32, 81] or designing loss functions based on deep features [95, 96]. Generative Adversarial Networks (GAN) have also been used for image blending [10, 23, 47, 77, 88, 101, 105]. For example, In-DomainGAN [101] exploits GAN inversion to achieve seamless blending, and StyleMap-GAN [47] blends images in the spatial latent space. Recently, SDEdit [61] proposes a blending method via diffusion models. The above learning-based methods tend to be more robust than pixel-based methods. But given two images with

large pose differences, they may struggle to preserve identity or generate unnatural effects,

In specific domains like faces [24, 63, 90] or hair [21, 49, 105, 106], multiple methods can swap and blend unaligned images. However, these methods are limited to faces or hair, and they often need 3D face morphable models [6, 31], or multi-view images [50, 62] to provide 3D information. Our method offers a general-purpose solution that can handle a diverse set of objects without the need for 3D data.

3D-aware generative models. Generative image models learn to synthesize realistic 2D images [16, 27, 33, 78, 85]. However, the original formulations do not account for the 3D nature of our visual world, making 3D manipulation difficult. Early 3D-aware GANs such as VON [104], Holo-GAN [64], and PlatonicGAN [37] use voxels-based GANs to represent and synthesize 3D content, but the high memory consumption of voxel representations limits their capacity for high-resolution synthesis.

Recently, several methods have integrated implicit scene representation, volumetric rendering, and GANs into generative NeRFs [12, 26, 65, 76]. Given a sampled viewpoint, an image is rendered via volumetric rendering and fed to a discriminator. For example, EG3D [11] uses a neural renderer with an efficient 3D representation called triplanes. StyleSDF [66] merges the style-based architecture and the SDF-based volume renderer. Multiple works [11, 34, 66, 100] have developed a two-stage model to generate high-resolution images. With GAN inversion methods [3, 25, 28, 30, 68, 72, 103, 107], we can utilize these 3D-aware generative models to align and blend images and produce view-consistent 3D effects.

3D-aware image editing. Classic 3D-aware image editing methods can create 3D effects given 2D photographs [18, 45, 46]. However, they often require manual efforts to reconstruct the input's geometry and texture. Recently, to reduce manual efforts, researchers have employed generative NeRFs for 3D-aware editing. For example, EditNeRF [59]
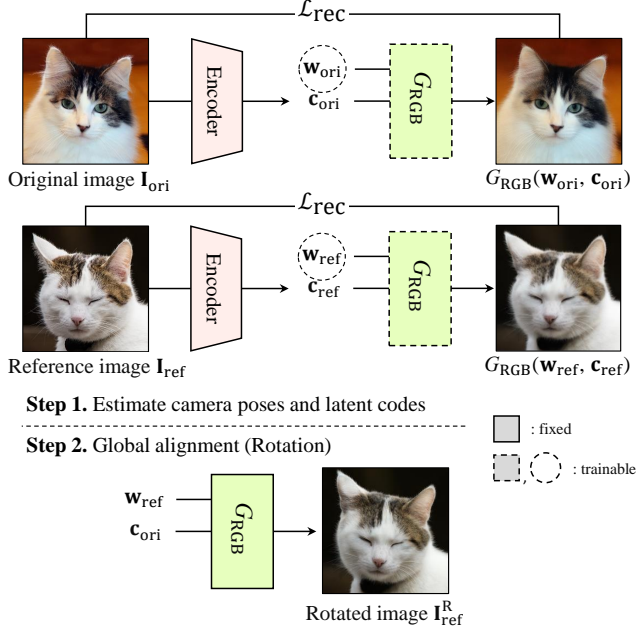
Figure 3. **Global alignment**: we first use a CNN encoder to infer the camera pose of each input image. **Step 1.** Given the camera pose, we estimate the latent code for each input using a reconstruction loss $\mathcal{L}_{rec}$. **Step 2.** Given the estimated camera pose c_{ori} and latent code w_{ref}, we rotate the reference image to match the pose of the original image.
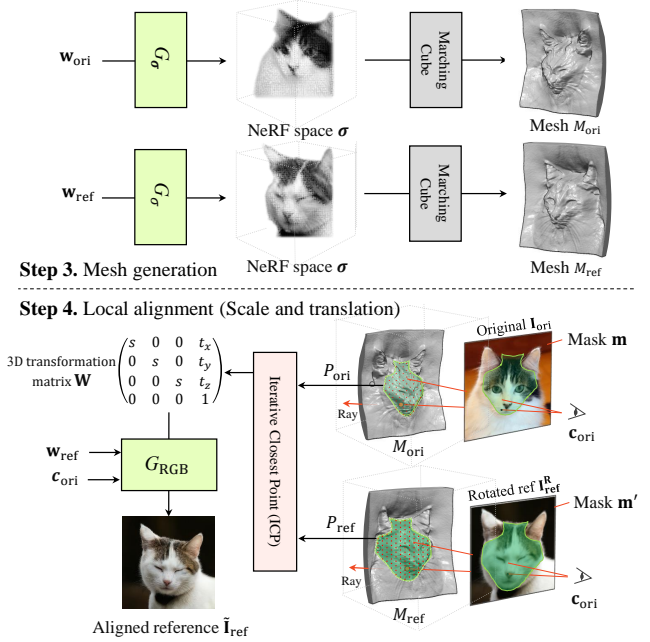

Figure 4. **Local alignment**: In **Step 3**, we first generate 3D meshes using the density field generator G_σ and the Marching Cube [60] algorithm. In **Step 4**, we calculate the intersected 3D points between the 2D mask m and the corresponding mesh M. Then, we use Iterative Closest Point (ICP) algorithm [4, 19] to estimate the 3D transformation matrix $\mathbf{W} \in \mathbb{R}^{4\times4}$ to align the 3D point clouds (P_{ori} and P_{ref}) in terms of the scale and the translation. Finally, we locally align the reference image $\tilde{I}_{ref}$ by $G_{RGB}(w_{ref}, c_{ori}; \mathbf{W})$.

uses separate latent codes to edit the shape and color of a NeRF object. NeRF-Editing [93] proposes to reflect geometric edits in implicit neural representations. CLIP-NeRF [86] uses a CLIP loss [71] to ensure that the edited result corresponds to the input condition. In SURF-GAN [54], they discover controllable attributes using NeRFs for training a 3D-controllable GAN. Kobayashi et al. [53] enable editing via semantic scene decomposition. While the above works tackle various image editing tasks, we focus on a different task – image blending, which requires both alignment and harmonization.

3. Method

We aim to perform 3D-aware image blending using only 2D images, with a user providing target masks for both original and reference images. Our method consists of two stages: 3D-aware alignment and 3D-aware blending. Before we blend, we first align a pair of images regarding the rotation, scale, and translation of objects. In Section 3.1, we describe *global alignment* for entire objects and *local alignment* for target regions of the objects. Then, we apply the 3D-aware blending method in the generative NeRF's latent space in Section 3.2. We use EG3D [11] as our backbone, although other 3D-aware generative models, such as StyleSDF [66], can also be applied. See Appendix F for more details.

3.1. 3D-aware alignment

Global alignment is an essential part of our blending method, as slight misalignment of two images in terms of rotation can make immense degradation in blending quality as shown in Figure 1. To match the reference image I_{ref}^{R} to the pose of the original image I_{ori}, we can use a generative NeRF generator G to estimate the camera pose c and the latent code w of each image. In *Step 1* in Figure 3, we first train a CNN encoder (*i.e.*, pose estimation network) to predict the camera poses of input images. During training, we can generate a large number of pairs of camera poses and images using generative NeRF and train the encoder using a reconstruction objective $\mathcal{L}_{rec}$ that contains L_1 and LPIPS [98]. With our encoder, we can estimate the camera poses c_{ori} and c_{ref} (defined as Euler angles $c \in SO3$) of the original and reference images, respectively. We only consider rotation as training images have often been aligned according to the scale and translation as part of the data preparation step for generative NeRFs.

Given the estimated camera poses, we project input images I_{ori} and I_{ref} to the latent codes w_{ori} and w_{ref} using Pivotal Tuning Inversion (PTI) [72]. We initialize the latent code as the mean latent code and optimize the latent codes and fine-
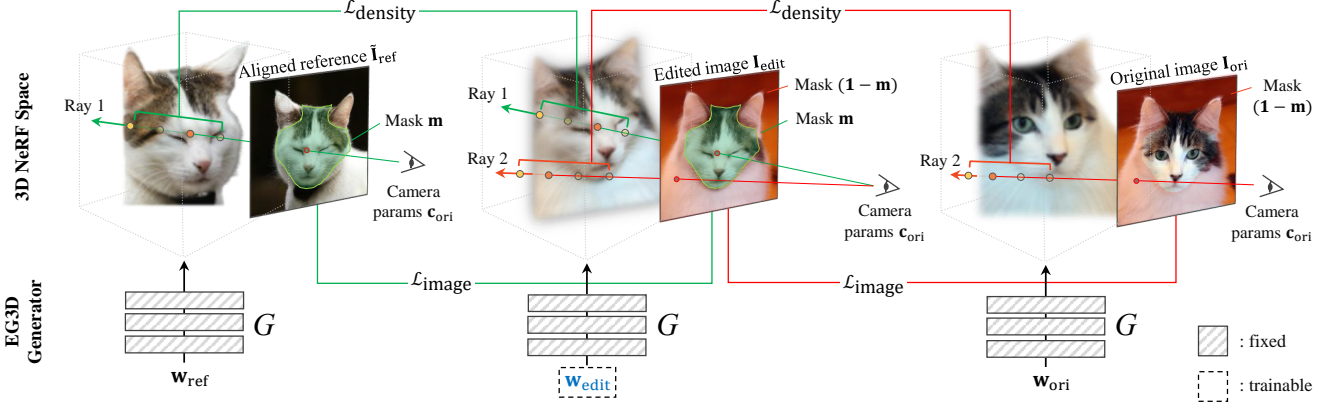
Figure 5. **Our 3D-aware blending pipeline.** Red and green lines denote the image-blending ($\mathcal{L}_{image}$) and density-blending losses ($\mathcal{L}_{density}$), respectively. Green rays pass through the interior of the mask ($\mathbf{m}$) and red rays pass through the exterior of the mask ($\mathbf{1} - \mathbf{m}$). $\mathcal{L}_{image}$ and $\mathcal{L}_{density}$ are used to optimize the latent code $\mathbf{w}_{edit}$ to generate the well-blended image I_{edit}.

tune the generator. Finally, as shown in *Step 2* of Figure 3, we can rotate the reference image I_{ref}^{R} as follows:

$$I_{ref}^{R} = G_{RGB}(\mathbf{w}_{ref}, \mathbf{c}_{ori}), \qquad (1)$$

where G_{RGB} is the image rendering function with the generative NeRF G. More details can be found in Appendix B.

Local alignment is a fine-grained alignment between the target regions of two images. Even though we have matched two images through global rotation, the scale and translation of target regions (*e.g.*, face, eyes, ears, *etc.*) need to be further aligned, as the location and size of each object part differ across two object instances. Figure 4 illustrates our local alignment algorithm. In *Step 3*, we need to obtain 3D meshes M_{ori} and M_{ref} of input images as follows:

$$M_{ori} = \mathbf{MC}(G_{\sigma}(\mathbf{w}_{ori})), \qquad (2)$$
$$M_{ref} = \mathbf{MC}(G_{\sigma}(\mathbf{w}_{ref})), \qquad (3)$$

where $\mathbf{MC}$ denotes the Marching Cube algorithm [60] and G_{σ} outputs the density field of a voxel grid$\in \mathbb{R}^{128 \times 128 \times 128}$.

In *Step 4* of Figure 4, we first cast rays through the interior of the target region $\mathbf{m}$ and determine the intersected 3D points with the mesh M_{ori}. We define the set of points as a 3D point cloud P_{ori}. Similarly, we can get the reference's 3D point cloud P_{ref}. The corresponding editing mask $\mathbf{m}'$ of reference can be automatically derived [38, 103] or specified by the users.

Given two sets of 3D point clouds P_{ref} and P_{ori}, we use the Iterative Closest Point (ICP) algorithm [4, 19] to obtain the 3D transformation matrix $\mathbf{W} \in \mathbb{R}^{4 \times 4}$. When we sample the 3D points to align the reference image, we transform the 3D point coordinates by multiplying the coordinate of sampled points with $\mathbf{W}$. We only use uniform scaling and translation in ICP, as we have already matched the global rotation as in the previous *global alignment* step. We discuss

the details in Appendix C. Finally, we can generate the fully aligned reference image $\tilde{I}_{ref}$ as follows:

$$\tilde{I}_{ref} = G_{RGB}(\mathbf{w}_{ref}, \mathbf{c}_{ori}; \mathbf{W}). \qquad (4)$$

3.2. 3D-aware blending

We aim to find the best latent code $\mathbf{w}_{edit}$ to synthesize a seamless and natural output. To achieve this goal, we exploit both 2D pixel constraints (RGB value) and 3D geometric constraints (volume density). With the proposed image-blending and density-blending losses, we optimize the latent code $\mathbf{w}_{edit}$. Algorithm details such as optimization latent spaces and input masks can be found in Appendix D.

Image-blending algorithms are often designed to match the color and details of the original image (*i.e.*, background) while preserving the structure of the reference image (*i.e.*, foreground) [70]. As shown in Figure 5, our image-blending loss matches the color and perceptual similarity of the original image using a combination of L_1 and LPIPS [98], while matching the reference image's details using LPIPS loss alone. Let I_{edit} be the rendered image from the latent code $\mathbf{w}_{edit}$. We define the image-blending loss as follows:

$$\begin{aligned} \mathcal{L}_{image} = & L_1((\mathbf{1} - \mathbf{m}) \circ I_{edit}, (\mathbf{1} - \mathbf{m}) \circ I_{ori}) \\ & + \lambda_1 \mathcal{L}_{LPIPS}((\mathbf{1} - \mathbf{m}) \circ I_{edit}, (\mathbf{1} - \mathbf{m}) \circ I_{ori}) \\ & + \lambda_2 \mathcal{L}_{LPIPS}(\mathbf{m} \circ I_{edit}, \mathbf{m} \circ I_{ref}), \qquad (5) \end{aligned}$$

where $\circ$ denotes element-wise multiplication. Here, λ_1 and λ_2 balance each loss term.

Density-blending is our key component in 3D-aware image blending. If we use only image-blending loss, the blending result easily falls blurry and can not reflect the reference object well. Especially, a highly structured object such as hair is hard to be blended in the 3D NeRF space without volume density information, as shown in Figure 7. By representing each image as a NeRF instance, we can calculate the density

σ of a given 3D location $\boldsymbol{x} \in \mathbb{R}^3$. Let $\mathcal{R}_{\text{ref}}$ and $\mathcal{R}_{\text{ori}}$ be the set of rays $\boldsymbol{r}$ passing through the interior and exterior of the target mask $\mathbf{m}$, respectively. For the 3D sample points along the rays $\mathcal{R}_{\text{ref}}$, we aim to match the density field between the reference and our output result, as shown as the bullet points in a green ray in Figure 5. For 3D sample points in $\mathcal{R}_{\text{ori}}$, we also match the densities between the original and our output result, as shown as the bullet points in a red ray in Figure 5. Let $G_{\sigma}(\mathbf{w}; \boldsymbol{x})$ be the density of a given 3D point $\boldsymbol{x}$ with a given latent code $\mathbf{w}$. Our density-blending loss can be formulated as follows:

$$\mathcal{L}_{\text{density}} = \sum_{\boldsymbol{r} \in \mathcal{R}_{\text{ref}}} \sum_{\boldsymbol{x} \in \boldsymbol{r}} L_1(G_{\sigma}(\mathbf{w}_{\text{edit}}; \boldsymbol{x}), G_{\sigma}(\mathbf{w}_{\text{ref}}; \boldsymbol{x}))$$
$$+ \sum_{\boldsymbol{r} \in \mathcal{R}_{\text{ori}}} \sum_{\boldsymbol{x} \in \boldsymbol{r}} L_1(G_{\sigma}(\mathbf{w}_{\text{edit}}; \boldsymbol{x}), G_{\sigma}(\mathbf{w}_{\text{ori}}; \boldsymbol{x})). \tag{6}$$

Our final objective function includes both image-blending loss and density-blending loss:

$$\mathcal{L} = \lambda \mathcal{L}_{\text{image}} + \mathcal{L}_{\text{density}}, \tag{7}$$

where λ is the hyperparameter that controls the contribution of the image-blending loss. If our user wants to blend the shape together without reflecting the color of reference, λ_2 in Eqn. 5 is set to 0. Otherwise, we can set λ_2 to a positive number to reflect the reference image's color and geometry as shown in Figure 8.

4. Experiments

In this section, we show the advantage of our full method over several existing methods and ablated baselines. In Section 4.1, we describe our experimental settings, including baselines, datasets, and evaluation metrics. In Section 4.2, we show both quantitative and qualitative comparisons. In addition to the automatic quantitative metrics, our user study shows that our method is preferred over baselines regarding photorealism. In Section 4.3, we analyze the effectiveness of each module via ablation studies. Lastly, Section 4.4 shows useful by-products of our method, such as generating multi-view images and controlling the color and geometry disentanglement. We provide experimental details in Appendix A and runtime of our method in Appendix B, C, and D.

4.1. Experimental setup

Baselines. We compare our method with various image blending methods using only 2D input images. For classic methods, we run Poisson blending [70], a widely-used gradient-domain editing method. We also compare with several recent learning-based methods [10, 42, 47, 61]. Latent Composition [10] utilizes the compositionality in GANs by finding the latent code of the roughly collaged inputs
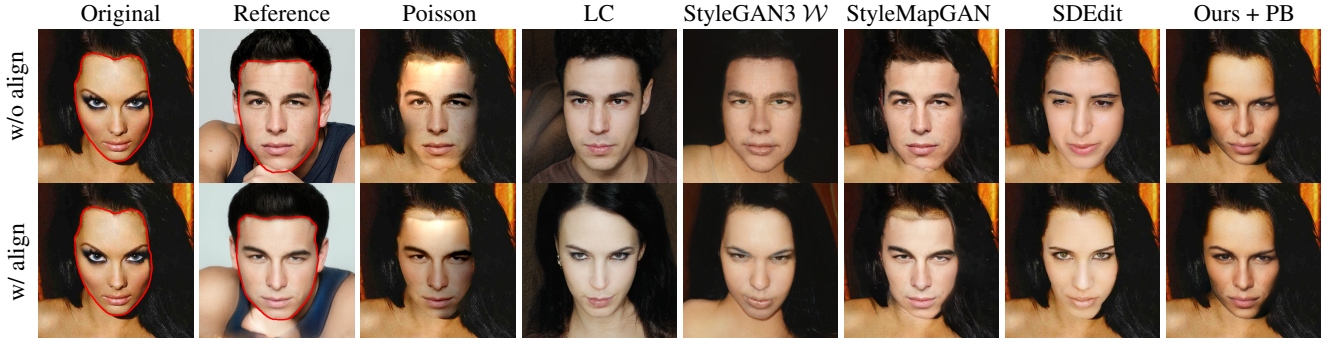
on the manifold of the generator. StyleMapGAN [47] proposes the spatial latent space for GANs to enable local parts blending by mixing the spatial latent codes. Recently, Karras *et al.* [42] proposed StyleGAN3, which provides rotation equivariance. Therefore, we additionally show their blending results by finding the latent code of the composited inputs on the StyleGAN3-R manifold. Both $\mathcal{W}$ and $\mathcal{W}+$ of StyleGAN3-R latent spaces are tested. SDEdit [61] is a diffusion-based blending method that produces a natural-looking result by denoising the corrupted image of a composite image.

Datasets. We use FFHQ [43] and AFHQv2-Cat datasets [20] for model training. For the loosely aligned dataset (AFHQ), we use both global and local alignment. For a strictly aligned dataset (FFHQ), we use global alignment.

To test blending performance, we use CelebA-HQ [41] for the FFHQ-trained models and AFHQv2-Cat test sets for the AFHQ-trained models. We randomly select 250 pairs of images from each dataset for an original and reference image. We also create a target mask for each pair to automatically simulate a user input using pretrained semantic segmentation networks [15, 91, 99]. We blend 5 and 3 semantic parts in each pair of images for CelebA-HQ and AFHQ, respectively. The total number of blended images is 1,250 (CelebA-HQ) and 750 (AFHQv2-Cat). We also include results on ShapeNet-Car dataset [13] to show that our method works well for non-facial data.

Evaluation metrics. For evaluation metrics, we use masked L_2, masked LPIPS [98] and Kernel Inception Score (KID) [5]. Masked L_2 (mL_2) is the L_2 distance between the original image and the blended image on the exterior of the mask, measuring the preservation of non-target areas of the original image. Unlike background regions, a pixel-wise loss is too strict for the target area to change during blending. We measure the perceptual similarity metric (LPIPS) [98] for the blended regions, which are called masked LPIPS (LPIPS$_m$) used in previous methods [39, 61]. Kernel Inception Score (KID) [5] is widely used to quantify the realism of the generated images regarding the real data distribution. We compute KID between blended images and the training dataset using the `clean-fid` library [69].

User study. To further examine the effectiveness of our 3D-aware blending method, we conduct a user study for photorealism. Our target goal is to edit the original image, so we exclude baselines that show highly flawed preservation of the original image. Human evaluates pairwise comparison of blended images between our method and one of the baselines. The user selects more real-looking images. We collect 2,500 comparison results via Amazon Mechanical Turk (MTurk). See Appendix G for more details.

Method	w/o align			w/ 3D-aware align		
	KID ↓	LPIPS_m ↓	$\text{m}L_2$ ↓	KID ↓	LPIPS_m ↓	$\text{m}L_2$ ↓
Poisson Blending [70]	<u>0.006</u>	0.4203	0.0069	<u>0.005</u>	0.2355	0.0051
Latent Composition [10]	0.012	0.4735	0.0388	0.012	0.4487	0.0321
StyleGAN3 $\mathcal{W}$ [42]	0.016	0.4379	0.0353	0.017	0.3921	0.0307
StyleGAN3 $\mathcal{W}+$ [42]	0.025	0.4634	0.0462	0.023	0.4086	0.0391
StyleMapGAN (32×32) [47]	0.007	0.3792	0.0118	0.006	<u>0.1989</u>	0.0045
SDEdit [61]	0.011	0.3857	0.0076	0.008	0.3427	**0.0003**
Ours	0.013	<u>0.2046</u>	<u>0.0050</u>	0.013	0.2046	0.0050
Ours + Poisson Blending	**0.002**	**0.1883**	**0.0007**	**0.002**	**0.1883**	<u>0.0007</u>

Table 1. **Comparison with baselines in the CelebA-HQ test set**. The first and second rows of the *figure* show the blending results without and with our 3D-aware alignment, respectively. Metric scores on the left side of the *table* show the results without alignment. We apply our 3D-aware alignment to the baselines on the right side of the table. Lower scores denote better performance in all metrics. The best and second-best scores are bold and underlined. Our method outperforms baselines in all metrics. LC and PB stand for Latent Composition [10] and Poisson Blending [70], respectively.

Method	w/o align			w/ 3D-aware align		
	KID ↓	LPIPS_m ↓	$\text{m}L_2$ ↓	KID ↓	LPIPS_m ↓	$\text{m}L_2$ ↓
Poisson Blending [70]	**0.002**	0.4956	<u>0.0024</u>	**0.002**	<u>0.2656</u>	**0.0004**
StyleGAN3 $\mathcal{W}$ [42]	0.006	0.4588	0.0316	0.006	0.3802	0.0268
StyleGAN3 $\mathcal{W}+$ [42]	0.014	0.4941	0.0298	0.013	0.3903	0.0236
StyleMapGAN (8×8) [47]	0.013	0.4840	0.0574	0.013	0.3221	0.0526
StyleMapGAN (16×16) [47]	0.006	0.4746	0.0225	0.004	0.2707	0.0160
Ours	0.005	<u>0.2739</u>	0.0073	0.005	0.2739	0.0073
Ours + Poisson Blending	**0.002**	**0.2229**	**0.0013**	**0.002**	**0.2229**	<u>0.0013</u>

Table 2. **Comparison with baselines in the AFHQv2-Cat test set**. Formats of the figure and table are the same as Table 1.

Method	CelebA-HQ		AFHQv2-Cat	
	w/o	w/ align	w/o	w/ align
Poisson [70]	80.9%	67.5%	87.6%	82.8%
StyleMap [47]	75.4%	66.3%	91.6%	83.6%
SDEdit [61]	61.1%	50.2%	N/A	N/A

Table 3. **User study** regarding the photorealism of the blended image. Baselines are selected with a good background preservation mL_2 score. The percentage denotes how often MTurk workers prefer our method to each baseline in pairwise comparison. Values larger than 50% mean ours outperforms the baseline.

4.2. Comparison with baselines

Here we compare our method with baselines in two variations. In the *w/o align* setting, we do not apply our 3D-aware alignment to baselines. In the *w/ align* setting, we align the reference image with our 3D-aware alignment. This experiment demonstrates the effectiveness of our proposed method. 1) Our alignment method consistently improves all baselines in all evaluation metrics: KID, LPIPS$_m$, and masked L_2. 2) Our 3D-aware blending method outperforms all baselines, including those that use our alignment method. We also report the combination of our method and Poisson blending to achieve better background preservation, as perfect inversion is still hard to be achieved in GAN-based methods. See Appendix E with an extra user study.

Table 1 shows comparison results in CelebA-HQ. The left side of the table includes all the baselines without our 3D-aware alignment. All metrics are worse than the right side of the table (w/ alignment). This result reveals that alignment between the original and reference image affects overall editing performance. Table 2 shows comparison results in AFHQv2-Cat. It shows the same tendency as Table 1. More comparison results are included in Appendix J.

Our method performs well regarding all metrics. Combined with Poisson blending, our method outperforms all baselines. Poisson blending and StyleMapGAN (16×16, 32×32) show great faithfulness to the input images but suffer from artifacts. Latent Composition, StyleMapGAN (8×8), and StyleGAN3 $\mathcal{W}$ produce realistic results but far from the input images. The identities of the original and reference images have changed, which is reflected by a worse LPIPS$_m$ and mL_2. SDEdit fails to reflect the reference image and shows worse LPIPS$_m$. StyleGAN3 $\mathcal{W}+$ often shows entirely collapsed images. Our method preserves the identity of the original image and reflects the reference image well while producing realistic outputs.

User study. We note that KID has a high correlation with background preservation. Unfortunately, it fails to capture the boundary artifacts and foreground image quality, especially for small foregrounds. To further evaluate the realism
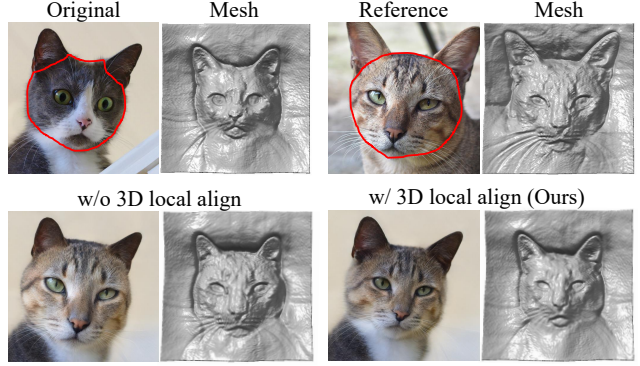

Figure 6. **The effect of the 3D local alignment**. Generative NeRF can align global poses, but cannot handle differences in local parts. For example, in AFHQ-Cat, the proportions of a cat's face and ears vary. (Bottom left) It cannot be handled with pose estimation only, so local parts can be blended in the wrong places. (Bottom right) Our 3D local alignment method alleviates this issue and produces more natural results.

score of results, we conduct a human perception study for our method and other baselines, which shows great preservation scores. As shown in Table 3, MTurk participants prefer our method to other baselines regarding the photorealism of the results. SDEdit with our 3D alignment shows a comparable realism score with ours, but it can not reflect the reference well, as reflected in worse LPIPS$_m$ score in Table 1. Similar to previous experiments, Mturk participants prefer baselines with alignment to their unaligned counterparts.

4.3. Ablation study

3D local alignment is an essential method in 3D-aware alignment as described in *Local alignment* of Section 3.1. Global alignment is a critical part, but it alone is not enough to handle loosely aligned images such as AFHQv2-Cat. Figure 6 shows an ablation study of our 3D local alignment method. The cat in the original image has a smaller face than the reference cat. If we just apply global alignment only, the blending result (bottom left in Figure 6) will create a much bigger face than humans normally expect. After locally aligning the face of the reference, we can obtain a natural-looking result with proper scale (bottom right in Figure 6). We provide an additional ablation study with a user study in Appendix C.

Density-blending loss gives rich 3D signals in the blending procedure. Section 3.2 explains how we can exploit volume density fields in blending. Delicate geometric structures, such as hair, can not be easily blended without awareness of 3D information. Figure 7 shows an ablation study of our density-blending loss. In the bottom left, the hair looks blurry in the blended image, and the mesh of the result shows shorter hair than that in the reference image. In the bottom right, the well-blended image and corresponding mesh show
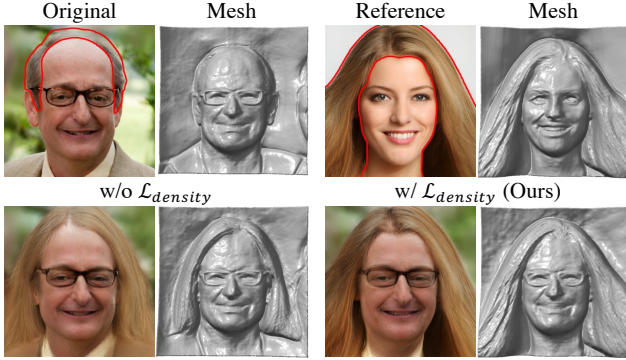
Figure 7. **The effect of our dense-blending loss** proposed in Section 3.2. Without the loss, 3D information is not considered, resulting in inaccurate blending in 3D space. In the bottom left figure, the hair mesh is not properly reflected without the density-blending loss, resulting in inaccurate blending and missing fine details.

Figure 8. **Color-geometry disentanglement with our model**. We can adjust the reflection of the reference image's color by adjusting the weight λ_2 in the image-blending loss. Without image blending loss on reference, we can focus on object shapes, as shown in the rightmost column.

that our density-blending loss contributes to capturing the highly structured object in blending. We provide an additional ablation study using StyleSDF [66] in Appendix F.

4.4. Additional advantages of NeRF-based blending

In addition to increasing blending quality, our 3D-aware method enables additional capacity: color-geometry disentanglement and multi-view consistent blending. As shown in Figure 8, we can control the influence of color in blending. The results with $\mathcal{L}_{\text{image}}$ have a redder color than the results without the loss. If we remove or assign a lower weight to the image-blending loss on reference (λ_2 in Eqn. 5), we can reflect the geometry of the reference object more than the color. In contrast, we can reflect colors better if we give a larger weight to λ_2. Note that we always use the image-blending loss on the original image to preserve it better. An additional ablation study using StyleSDF is included in Appendix F.

A key component of generative NeRFs is multi-view consistent generation. After applying the blending procedure described in Section 3.2, we have an optimized latent code $\mathbf{w}_{\text{edit}}$. Generative NeRF can synthesize a novel view blended image using $\mathbf{w}_{\text{edit}}$ and a target camera pose. Figure 9 shows the view-consistent blended results in CelebA-HQ, AFHQv2-Cat, and ShapeNet-Car [13]. We provide more multi-view results for EG3D and StyleSDF in Appendix J.

5. Discussion and Limitations

Our method exploits the capability of NeRFs to align and blend images in a 3D-aware manner only with a collection of 2D images. Our 3D-aware alignment boosts the quality of existing 2D baselines. 3D-aware blending exceeds improved 2D baselines with our alignment method and shows additional advantages such as color-geometry disentanglement and multi-view consistent blending. We hope our approach paves the road to 3D-aware blending.
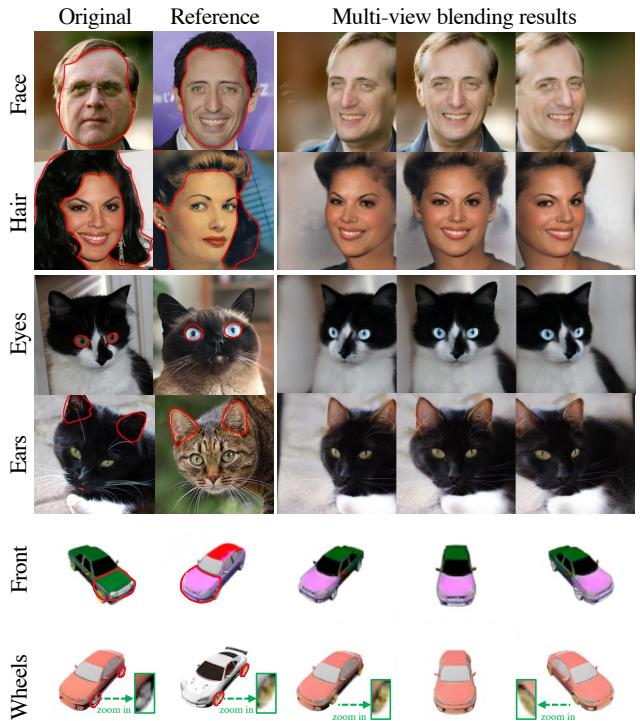

Figure 9. **Multi-view blending results** in various datasets: CelebA-HQ, AFHQv2-Cat, and ShapeNet-Car. Since we optimize the latent code of the generative NeRF, we can sample images of the blended object in different poses through the usual sampling process of the generative NeRF.

Despite improvements over existing blending baselines, several limitations still exist in our approach. First, our method depends on GAN inversion, which is a bottleneck of the overall performance regarding quality and speed. Second, the ICP algorithm in our 3D alignment occasionally yields incorrect 3D alignment. These problems can be mitigated by the new advances [52, 87] in 3D-aware GAN inversion and 3D alignment. See Appendix H for more discussion.

References

[1] Aseem Agarwala, Mira Dontcheva, Maneesh Agrawala, Steven Drucker, Alex Colburn, Brian Curless, David Salesin, and Michael Cohen. Interactive digital photomontage. In *ACM SIGGRAPH*. 2004. 2

[2] Dmitry Baranchuk, Ivan Rubachev, Andrey Voynov, Valentin Khrulkov, and Artem Babenko. Label-efficient semantic segmentation with diffusion models. In *International Conference on Learning Representations (ICLR)*, 2022. 13

[3] David Bau, Hendrik Strobelt, William Peebles, Jonas Wulff, Bolei Zhou, Jun-Yan Zhu, and Antonio Torralba. Semantic photo manipulation with a generative image prior. *arXiv preprint arXiv:2005.07727*, 2020. 2

[4] Paul J Besl and Neil D McKay. Method for registration of 3-d shapes. In *Sensor fusion IV: control paradigms and data structures*, 1992. 3, 4, 14, 18

[5] Mikołaj Bińkowski, Danica J. Sutherland, Michael Arbel, and Arthur Gretton. Demystifying mmd gans. In *International Conference on Learning Representations (ICLR)*, 2018. 5

[6] Volker Blanz and Thomas Vetter. A morphable model for the synthesis of 3d faces. In *Proceedings of the 26th annual conference on Computer graphics and interactive techniques*, 1999. 2

[7] G. Bradski. The OpenCV Library. *Dr. Dobb's Journal of Software Tools*, 2000. 13

[8] Matthew Brown, David G Lowe, et al. Recognising panoramas. In *IEEE International Conference on Computer Vision (ICCV)*, 2003. 2

[9] Peter J Burt and Edward H Adelson. The laplacian pyramid as a compact image code. In *Readings in computer vision*. 1987. 1, 2

[10] Lucy Chai, Jonas Wulff, and Phillip Isola. Using latent space regression to analyze and leverage compositionality in gans. In *International Conference on Learning Representations (ICLR)*, 2021. 2, 5, 6, 13, 16, 21

[11] Eric R. Chan, Connor Z. Lin, Matthew A. Chan, Koki Nagano, Boxiao Pan, Shalini De Mello, Orazio Gallo, Leonidas Guibas, Jonathan Tremblay, Sameh Khamis, Tero Karras, and Gordon Wetzstein. Efficient geometry-aware 3D generative adversarial networks. In *IEEE Conference on Computer Vision and Pattern Recognition (CVPR)*, 2022. 1, 2, 3, 13, 14, 17

[12] Eric R Chan, Marco Monteiro, Petr Kellnhofer, Jiajun Wu, and Gordon Wetzstein. pi-gan: Periodic implicit generative adversarial networks for 3d-aware image synthesis. In *IEEE Conference on Computer Vision and Pattern Recognition (CVPR)*, 2021. 1, 2

[13] Angel X Chang, Thomas Funkhouser, Leonidas Guibas, Pat Hanrahan, Qixing Huang, Zimo Li, Silvio Savarese, Manolis Savva, Shuran Song, Hao Su, et al. Shapenet: An information-rich 3d model repository. *arXiv preprint arXiv:1512.03012*, 2015. 5, 8, 13, 23

[14] Bor-Chun Chen and Andrew Kae. Toward realistic image compositing with adversarial learning. In *IEEE Conference on Computer Vision and Pattern Recognition (CVPR)*, 2019. 1

[15] Liang-Chieh Chen, George Papandreou, Florian Schroff, and Hartwig Adam. Rethinking atrous convolution for semantic image segmentation. *arXiv preprint arXiv:1706.05587*, 2017. 5

[16] Mark Chen, Alec Radford, Rewon Child, Jeffrey Wu, Heewoo Jun, David Luan, and Ilya Sutskever. Generative pretraining from pixels. In *International Conference on Machine Learning (ICML)*, 2020. 2

[17] Tao Chen, Ming-Ming Cheng, Ping Tan, Ariel Shamir, and Shi-Min Hu. Sketch2photo: Internet image montage. *ACM Transactions on graphics (TOG)*, 2009. 2

[18] Tao Chen, Zhe Zhu, Ariel Shamir, Shi-Min Hu, and Daniel Cohen-Or. 3-sweep: Extracting editable objects from a single photo. *ACM Transactions on graphics (TOG)*, 2013. 2

[19] Yang Chen and Gérard Medioni. Object modelling by registration of multiple range images. *Image and vision computing*, 1992. 3, 4, 14, 18

[20] Yunjey Choi, Youngjung Uh, Jaejun Yoo, and Jung-Woo Ha. Stargan v2: Diverse image synthesis for multiple domains. In *IEEE Conference on Computer Vision and Pattern Recognition (CVPR)*, 2020. 5, 13, 16, 18

[21] Chaeyeon Chung, Taewoo Kim, Hyelin Nam, Seunghwan Choi, Gyojung Gu, Sunghyun Park, and Jaegul Choo. Hairfit: pose-invariant hairstyle transfer via flow-based hair alignment and semantic-region-aware inpainting. In *The British Machine Vision Conference (BMVC)*, 2021. 2

[22] Edo Collins, Raja Bala, Bob Price, and Sabine Susstrunk. Editing in style: Uncovering the local semantics of gans. In *IEEE Conference on Computer Vision and Pattern Recognition (CVPR)*, 2020. 2

[23] Edo Collins, Raja Bala, Bob Price, and Sabine Susstrunk. Editing in style: Uncovering the local semantics of gans. In *IEEE Conference on Computer Vision and Pattern Recognition (CVPR)*, 2020. 2

[24] Kevin Dale, Kalyan Sunkavalli, Micah K Johnson, Daniel Vlasic, Wojciech Matusik, and Hanspeter Pfister. Video face replacement. In *ACM SIGGRAPH Asia*, 2011. 2

[25] Giannis Daras, Wen-Sheng Chu, Abhishek Kumar, Dmitry Lagun, and Alexandros G Dimakis. Solving inverse problems with nerfgans. *arXiv preprint arXiv:2112.09061*, 2021. 2

[26] Yu Deng, Jiaolong Yang, Jianfeng Xiang, and Xin Tong. Gram: Generative radiance manifolds for 3d-aware image generation. In *IEEE Conference on Computer Vision and Pattern Recognition (CVPR)*, 2022. 2

[27] Prafulla Dhariwal and Alexander Nichol. Diffusion models beat gans on image synthesis. In *Conference on Neural Information Processing Systems (NeurIPS)*, 2021. 2, 13

[28] Tan M Dinh, Anh Tuan Tran, Rang Nguyen, and Binh-Son Hua. Hyperinverter: Improving stylegan inversion via hypernetwork. In *IEEE Conference on Computer Vision and Pattern Recognition (CVPR)*, 2022. 2

[29] Zeev Farbman, Gil Hoffer, Yaron Lipman, Daniel Cohen-Or, and Dani Lischinski. Coordinates for instant image cloning. *ACM Transactions on graphics (TOG)*, 2009. 2

[30] Qianli Feng, Viraj Shah, Raghudeep Gadde, Pietro Perona, and Aleix Martinez. Near perfect gan inversion. *arXiv preprint arXiv:2202.11833*, 2022. 2

[31] Claudio Ferrari, Stefano Berretti, Pietro Pala, and Alberto Del Bimbo. A sparse and locally coherent morphable face model for dense semantic correspondence across heterogeneous 3d faces. *IEEE Transactions on Pattern Analysis and Machine Intelligence (TPAMI)*, 2021. 2

[32] Anna Frühstück, Ibraheem Alhashim, and Peter Wonka. Tilegan: synthesis of large-scale non-homogeneous textures. *ACM Transactions on graphics (TOG)*, 2019. 2

[33] Ian Goodfellow, Jean Pouget-Abadie, Mehdi Mirza, Bing Xu, David Warde-Farley, Sherjil Ozair, Aaron Courville, and Yoshua Bengio. Generative adversarial networks. In *Conference on Neural Information Processing Systems (NeurIPS)*, 2014. 2

[34] Jiatao Gu, Lingjie Liu, Peng Wang, and Christian Theobalt. Stylenerf: A style-based 3d-aware generator for high-resolution image synthesis. In *International Conference on Learning Representations (ICLR)*, 2022. 1, 2

[35] Jeffrey T Hancock and Jeremy N Bailenson. The social impact of deepfakes. *Cyberpsychology, behavior, and social networking*, 2021. 19

[36] James Hays and Alexei A Efros. Scene completion using millions of photographs. *ACM Transactions on graphics (TOG)*, 2007. 1, 2

[37] Philipp Henzler, Niloy J Mitra, and Tobias Ritschel. Escaping plato's cave: 3d shape from adversarial rendering. In *IEEE International Conference on Computer Vision (ICCV)*, 2019. 2

[38] Berthold K.P. Horn and Brian G. Schunck. Determining optical flow. *Artificial Intelligence*, 1981. 4, 16

[39] Minyoung Huh, Richard Zhang, Jun-Yan Zhu, Sylvain Paris, and Aaron Hertzmann. Transforming and projecting images into class-conditional generative networks. In *Computer Vision–ECCV 2020: 16th European Conference, Glasgow, UK, August 23–28, 2020, Proceedings, Part II 16*, pages 17–34. Springer, 2020. 5

[40] Jiaya Jia, Jian Sun, Chi-Keung Tang, and Heung-Yeung Shum. Drag-and-drop pasting. In *ACM Transactions on graphics (TOG)*, 2006. 2

[41] Tero Karras, Timo Aila, Samuli Laine, and Jaakko Lehtinen. Progressive growing of gans for improved quality, stability, and variation. In *International Conference on Learning Representations (ICLR)*, 2018. 5, 18

[42] Tero Karras, Miika Aittala, Samuli Laine, Erik Härkönen, Janne Hellsten, Jaakko Lehtinen, and Timo Aila. Alias-free generative adversarial networks. In *Conference on Neural Information Processing Systems (NeurIPS)*, 2021. 5, 6, 13, 16

[43] Tero Karras, Samuli Laine, and Timo Aila. A style-based generator architecture for generative adversarial networks. In *IEEE Conference on Computer Vision and Pattern Recognition (CVPR)*, 2019. 5, 13

[44] Tero Karras, Samuli Laine, Miika Aittala, Janne Hellsten, Jaakko Lehtinen, and Timo Aila. Analyzing and improving the image quality of stylegan. In *IEEE Conference on Computer Vision and Pattern Recognition (CVPR)*, 2020. 13

[45] Kevin Karsch, Varsha Hedau, David Forsyth, and Derek Hoiem. Rendering synthetic objects into legacy photographs. *ACM Transactions on graphics (TOG)*, 2011. 2

[46] Natasha Kholgade, Tomas Simon, Alexei Efros, and Yaser Sheikh. 3d object manipulation in a single photograph using stock 3d models. *ACM Transactions on graphics (TOG)*, 2014. 2

[47] Hyunsu Kim, Yunjey Choi, Junho Kim, Sungjoo Yoo, and Youngjung Uh. Exploiting spatial dimensions of latent in gan for real-time image editing. In *IEEE Conference on Computer Vision and Pattern Recognition (CVPR)*, 2021. 1, 2, 5, 6, 7, 13, 16

[48] Hanjoo Kim, Minkyu Kim, Dongjoo Seo, Jinwoong Kim, Heungseok Park, Soeun Park, Hyunwoo Jo, KyungHyun Kim, Youngil Yang, Youngkwan Kim, et al. Nsml: Meet the mlaas platform with a real-world case study. *arXiv preprint arXiv:1810.09957*, 2018. 9

[49] Taewoo Kim, Chaeyeon Chung, Yoonseo Kim, Sunghyun Park, Kangyeol Kim, and Jaegul Choo. Style your hair: Latent optimization for pose-invariant hairstyle transfer via local-style-aware hair alignment. In *European Conference on Computer Vision (ECCV)*, 2022. 2

[50] Taewoo Kim, Chaeyeon Chung, Sunghyun Park, Gyojung Gu, Keonmin Nam, Wonzo Choe, Jaesung Lee, and Jaegul Choo. K-hairstyle: A large-scale korean hairstyle dataset for virtual hair editing and hairstyle classification. In *IEEE International Conference on Image Processing (ICIP)*, 2021. 2

[51] Diederik P Kingma and Jimmy Ba. Adam: A method for stochastic optimization. In *International Conference on Learning Representations (ICLR)*, 2015. 13

[52] Jaehoon Ko, Kyusun Cho, Daewon Choi, Kwangrok Ryoo, and Seungryong Kim. 3d gan inversion with pose optimization. *WACV*, 2023. 8, 19

[53] Sosuke Kobayashi, Eiichi Matsumoto, and Vincent Sitzmann. Decomposing nerf for editing via feature field distillation. *arXiv preprint arXiv:2205.15585*, 2022. 3

[54] Jeong-gi Kwak, Yuanming Li, Dongsik Yoon, Donghyeon Kim, David Han, and Hanseok Ko. Injecting 3d perception of controllable nerf-gan into stylegan for editable portrait image synthesis. In *European Conference on Computer Vision (ECCV)*, 2022. 3

[55] Vivek Kwatra, Arno Schödl, Irfan Essa, Greg Turk, and Aaron Bobick. Graphcut textures: Image and video synthesis using graph cuts. *ACM Transactions on graphics (TOG)*, 2003. 1, 2

[56] Jean-François Lalonde, Derek Hoiem, Alexei A Efros, Carsten Rother, John Winn, and Antonio Criminisi. Photo clip art. *ACM Transactions on graphics (TOG)*, 2007. 2

[57] Anat Levin, Dani Lischinski, and Yair Weiss. A closed-form solution to natural image matting. *IEEE Transactions on Pattern Analysis and Machine Intelligence (TPAMI)*, 2007. 2

[58] Chen-Hsuan Lin, Ersin Yumer, Oliver Wang, Eli Shechtman, and Simon Lucey. St-gan: Spatial transformer generative adversarial networks for image compositing. In *IEEE Conference on Computer Vision and Pattern Recognition (CVPR)*, 2018. 1

[59] Steven Liu, Xiuming Zhang, Zhoutong Zhang, Richard Zhang, Jun-Yan Zhu, and Bryan Russell. Editing conditional radiance fields. In *IEEE International Conference on Computer Vision (ICCV)*, 2021. 2

[60] William E Lorensen and Harvey E Cline. Marching cubes: A high resolution 3d surface construction algorithm. *ACM Transactions on graphics (TOG)*, 1987. 3, 4

[61] Chenlin Meng, Yutong He, Yang Song, Jiaming Song, Jiajun Wu, Jun-Yan Zhu, and Stefano Ermon. Sdedit: Guided image synthesis and editing with stochastic differential equations. In *International Conference on Learning Representations (ICLR)*, 2021. 1, 2, 5, 6, 7, 13, 16, 18

[62] Arsha Nagrani, Joon Son Chung, and Andrew Zisserman. Voxceleb: a large-scale speaker identification dataset. In *INTERSPEECH*, 2017. 2

[63] Thanh Thi Nguyen, Quoc Viet Hung Nguyen, Dung Tien Nguyen, Duc Thanh Nguyen, Thien Huynh-The, Saeid Nahavandi, Thanh Tam Nguyen, Quoc-Viet Pham, and Cuong M Nguyen. Deep learning for deepfakes creation and detection: A survey. *Computer Vision and Image Understanding*, 2022. 2

[64] Thu Nguyen-Phuoc, Chuan Li, Lucas Theis, Christian Richardt, and Yong-Liang Yang. Hologan: Unsupervised learning of 3d representations from natural images. In *IEEE International Conference on Computer Vision (ICCV)*, 2019. 2

[65] Michael Niemeyer and Andreas Geiger. Giraffe: Representing scenes as compositional generative neural feature fields. In *IEEE Conference on Computer Vision and Pattern Recognition (CVPR)*, 2021. 2

[66] Roy Or-El, Xuan Luo, Mengyi Shan, Eli Shechtman, Jeong Joon Park, and Ira Kemelmacher-Shlizerman. Stylesdf: High-resolution 3d-consistent image and geometry generation. In *IEEE Conference on Computer Vision and Pattern Recognition (CVPR)*, 2022. 2, 3, 8, 17, 23

[67] Xingang Pan, Xudong Xu, Chen Change Loy, Christian Theobalt, and Bo Dai. A shading-guided generative implicit model for shape-accurate 3d-aware image synthesis. *Conference on Neural Information Processing Systems (NeurIPS)*, 2021. 1

[68] Gaurav Parmar, Yijun Li, Jingwan Lu, Richard Zhang, Jun-Yan Zhu, and Krishna Kumar Singh. Spatially-adaptive multilayer selection for gan inversion and editing. In *Proceedings of the IEEE/CVF Conference on Computer Vision and Pattern Recognition*, pages 11399–11409, 2022. 2

[69] Gaurav Parmar, Richard Zhang, and Jun-Yan Zhu. On aliased resizing and surprising subtleties in gan evaluation. In *Proceedings of the IEEE/CVF Conference on Computer Vision and Pattern Recognition*, pages 11410–11420, 2022. 5

[70] Patrick Pérez, Michel Gangnet, and Andrew Blake. Poisson image editing. In *ACM SIGGRAPH*, 2003. 1, 2, 4, 5, 6, 7, 13, 16, 17, 21

[71] Alec Radford, Jong Wook Kim, Chris Hallacy, Aditya Ramesh, Gabriel Goh, Sandhini Agarwal, Girish Sastry, Amanda Askell, Pamela Mishkin, Jack Clark, et al. Learning transferable visual models from natural language supervision. In *International Conference on Machine Learning (ICML)*, 2021. 3

[72] Daniel Roich, Ron Mokady, Amit H Bermano, and Daniel Cohen-Or. Pivotal tuning for latent-based editing of real images. *ACM Transactions on graphics (TOG)*, 2022. 2, 3, 14

[73] Carsten Rother, Vladimir Kolmogorov, and Andrew Blake. " grabcut" interactive foreground extraction using iterated graph cuts. *ACM Transactions on graphics (TOG)*, 2004. 2

[74] Tim Salimans, Ian Goodfellow, Wojciech Zaremba, Vicki Cheung, Alec Radford, and Xi Chen. Improved techniques for training gans. In *Conference on Neural Information Processing Systems (NeurIPS)*, 2016. 14

[75] Othman Sbai, Camille Couprie, and Mathieu Aubry. Surprising image compositions. In *IEEE Conference on Computer Vision and Pattern Recognition (CVPR) Workshop*, 2021. 1

[76] Katja Schwarz, Yiyi Liao, Michael Niemeyer, and Andreas Geiger. Graf: Generative radiance fields for 3d-aware image synthesis. *Conference on Neural Information Processing Systems (NeurIPS)*, 2020. 1, 2

[77] Yichun Shi, Xiao Yang, Yangyue Wan, and Xiaohui Shen. Semanticstylegan: Learning compositional generative priors for controllable image synthesis and editing. In *IEEE Conference on Computer Vision and Pattern Recognition (CVPR)*, 2022. 2

[78] Yang Song, Jascha Sohl-Dickstein, Diederik P Kingma, Abhishek Kumar, Stefano Ermon, and Ben Poole. Score-based generative modeling through stochastic differential equations. In *International Conference on Learning Representations (ICLR)*, 2021. 2

[79] Nako Sung, Minkyu Kim, Hyunwoo Jo, Youngil Yang, Jingwoong Kim, Leonard Lausen, Youngkwan Kim, Gayoung Lee, Donghyun Kwak, Jung-Woo Ha, et al. Nsml: A machine learning platform that enables you to focus on your models. *arXiv preprint arXiv:1712.05902*, 2017. 9

[80] Kalyan Sunkavalli, Micah K Johnson, Wojciech Matusik, and Hanspeter Pfister. Multi-scale image harmonization. *ACM Transactions on Graphics (TOG)*, 29(4):1–10, 2010. 2

[81] Ryohei Suzuki, Masanori Koyama, Takeru Miyato, Taizan Yonetsuji, and Huachun Zhu. Spatially controllable image synthesis with internal representation collaging. In *arXiv preprint arXiv:1811.10153*, 2018. 2

[82] Richard Szeliski, Matthew Uyttendaele, and Drew Steedly. Fast poisson blending using multi-splines. In *IEEE International Conference on Computational Photography (ICCP)*, 2011. 2

[83] Michael W Tao, Micah K Johnson, and Sylvain Paris. Error-tolerant image compositing. In *European Conference on Computer Vision (ECCV)*, 2010. 2

[84] Matthew Uyttendaele, Ashley Eden, and Richard Skeliski. Eliminating ghosting and exposure artifacts in image mosaics. In *Proceedings of the 2001 IEEE Computer Society Conference on Computer Vision and Pattern Recognition (CVPR)*, 2001. 1

[85] Aaron Van den Oord, Nal Kalchbrenner, Lasse Espeholt, Oriol Vinyals, Alex Graves, et al. Conditional image generation with pixelcnn decoders. *Conference on Neural Information Processing Systems (NeurIPS)*, 2016. 2

[86] Can Wang, Menglei Chai, Mingming He, Dongdong Chen, and Jing Liao. Clip-nerf: Text-and-image driven manipulation of neural radiance fields. In *IEEE Conference on Computer Vision and Pattern Recognition (CVPR)*, 2022. 3

[87] Yue Wang and Justin M. Solomon. Deep closest point: Learning representations for point cloud registration. In *IEEE International Conference on Computer Vision (ICCV)*, October 2019. 8, 18, 19

[88] Huikai Wu, Shuai Zheng, Junge Zhang, and Kaiqi Huang. Gp-gan: Towards realistic high-resolution image blending. In *ACM international conference on multimedia (ACM-MM)*, 2019. 1, 2

[89] Su Xue, Aseem Agarwala, Julie Dorsey, and Holly Rushmeier. Understanding and improving the realism of image composites. *ACM Transactions on graphics (TOG)*, 31(4):1–10, 2012. 2

[90] Fei Yang, Jue Wang, Eli Shechtman, Lubomir Bourdev, and Dimitri Metaxas. Expression flow for 3d-aware face component transfer. In *ACM SIGGRAPH*, 2011. 2

[91] Changqian Yu, Jingbo Wang, Chao Peng, Changxin Gao, Gang Yu, and Nong Sang. Bisenet: Bilateral segmentation network for real-time semantic segmentation. In *European Conference on Computer Vision (ECCV)*, 2018. 5

[92] Ning Yu, Larry S Davis, and Mario Fritz. Attributing fake images to gans: Learning and analyzing gan fingerprints. In *IEEE International Conference on Computer Vision (ICCV)*, 2019. 19

[93] Yu-Jie Yuan, Yang-Tian Sun, Yu-Kun Lai, Yuewen Ma, Rongfei Jia, and Lin Gao. Nerf-editing: geometry editing of neural radiance fields. In *IEEE Conference on Computer Vision and Pattern Recognition (CVPR)*, 2022. 3

[94] Fangneng Zhan, Hongyuan Zhu, and Shijian Lu. Spatial fusion gan for image synthesis. In *IEEE Conference on Computer Vision and Pattern Recognition (CVPR)*, 2019. 1

[95] He Zhang, Jianming Zhang, Federico Perazzi, Zhe Lin, and Vishal M Patel. Deep image compositing. In *Winter Conference on Applications of Computer Vision (WACV)*, 2021. 2

[96] Lingzhi Zhang, Tarmily Wen, and Jianbo Shi. Deep image blending. In *Winter Conference on Applications of Computer Vision (WACV)*, 2020. 2

[97] Richard Zhang, Phillip Isola, and Alexei A Efros. Colorful image colorization. In *European Conference on Computer Vision (ECCV)*, 2016. 18

[98] Richard Zhang, Phillip Isola, Alexei A Efros, Eli Shechtman, and Oliver Wang. The unreasonable effectiveness of deep features as a perceptual metric. In *IEEE Conference on Computer Vision and Pattern Recognition (CVPR)*, 2018. 3, 4, 5, 13, 14

[99] Yuxuan Zhang, Huan Ling, Jun Gao, Kangxue Yin, Jean-Francois Lafleche, Adela Barriuso, Antonio Torralba, and Sanja Fidler. Datasetgan: Efficient labeled data factory with minimal human effort. In *IEEE Conference on Computer Vision and Pattern Recognition (CVPR)*, 2021. 5

[100] Peng Zhou, Lingxi Xie, Bingbing Ni, and Qi Tian. Cips-3d: A 3d-aware generator of gans based on conditionally-independent pixel synthesis. *arXiv preprint arXiv:2110.09788*, 2021. 1, 2

[101] Jiapeng Zhu, Yujun Shen, Deli Zhao, and Bolei Zhou. In-domain gan inversion for real image editing. In *European Conference on Computer Vision (ECCV)*, 2020. 2

[102] Jun-Yan Zhu, Philipp Krahenbuhl, Eli Shechtman, and Alexei A Efros. Learning a discriminative model for the perception of realism in composite images. In *IEEE International Conference on Computer Vision (ICCV)*, 2015. 1

[103] Jun-Yan Zhu, Philipp Krähenbühl, Eli Shechtman, and Alexei A. Efros. Generative visual manipulation on the natural image manifold. In *European Conference on Computer Vision (ECCV)*, 2016. 2, 4, 16

[104] Jun-Yan Zhu, Zhoutong Zhang, Chengkai Zhang, Jiajun Wu, Antonio Torralba, Josh Tenenbaum, and Bill Freeman. Visual object networks: Image generation with disentangled 3d representations. *Conference on Neural Information Processing Systems (NeurIPS)*, 2018. 2

[105] Peihao Zhu, Rameen Abdal, John Femiani, and Peter Wonka. Barbershop: Gan-based image compositing using segmentation masks. In *ACM Transactions on graphics (TOG)*, 2021. 1, 2

[106] Peihao Zhu, Rameen Abdal, John Femiani, and Peter Wonka. Hairnet: Hairstyle transfer with pose changes. In *European Conference on Computer Vision (ECCV)*, 2022. 1, 2

[107] Peihao Zhu, Rameen Abdal, Yipeng Qin, John Femiani, and Peter Wonka. Improved stylegan embedding: Where are the good latents? *arXiv preprint arXiv:2012.09036*, 2020. 2

Overview of Appendix.

- Please refer to the code, data, and results on our website: https://blandocs.github.io/blendnerf.

- Experimental details are described in Appendix A.

- Details of inversion are described in Appendix B.

- Details of local alignment are described in Appendix C with an extra user study.

- Details of 3D-aware blending are described in Appendix D.

- Combination of our method and Poisson blending is described in Appendix E with an extra user study.

- 3D-aware blending in StyleSDF is described in Appendix F. Our method can be applied to Signed Distance Fields (SDF) beyond NeRFs.

- Details of user studies are described in Appendix G.

- Failure cases are described in Appendix H.

- Societal impact is discussed in Appendix I.

- Additional qualitative results are in Appendix J.

A. Experimental details

Baselines.

- **Poisson Blending** [70] is implemented in OpenCV [7]. We use `cv2.seamlessClone` in the `cv2.NORMAL_CLONE` cloning type.

- **StyleGAN3**: As there is no official projection code in StyleGAN3 [42], we use unofficial implementation[1]. We follow the hyperparameters of StyleGAN2 [44] official projection algorithm[2] and set the number of optimization iterations as 1,000.

- **StyleMapGAN** [47] introduce *stylemap*, which has spatial dimensions in the latent space. We use the official pretrained networks with 8×8 and 16×16 *stylemap* for AFHQ [20] and 32×32 *stylemap* for FFHQ [43].

- **SDEdit** [61] transforms a noise-added image into a realistic image through iterative denoising. The total denoising step is a sensitive hyperparameter that decides blending quality. If it is too small, blended results are faithful to the input images but less realistic. If it is too large, blended results are less faithful to the input images but more realistic. We carefully select the

number of iterations for the best quality; 300 for the small editing parts (eyes, nose, and lip) and 500 for the large editing parts (face and hair). To exploit the FFHQ-pretrained model [2][3], we implement guided-diffusion [27] version of SDEdit.

- **Latent Composition** [10] requires a mask to decide which area preserve. In our blending experiment, we need to preserve both the original and reference image, so we use a mask for the entire image.

Datasets. We select FFHQ [43] and AFHQv2-Cat [20] for our comparison experiments. FFHQ has 1024×1024 images, and AFHQ has 512×512 images. In SDEdit [2,61], the pretrained model is trained on 256×256 FFHQ. Our backbone network EG3D [11] is trained on 512×512 FFHQ. In Table 1, we upsample the blending results of SDEdit and EG3D using bilinear interpolation for a fair comparison. Other baselines in FFHQ and all methods in AFHQ have the same resolution with the corresponding datasets. As the StyleMapGAN network is trained on AFHQv1, we fine-tune the networks using AFHQv2-Cat. As EG3D uses a different crop version of FFHQ compared to the original FFHQ, we fine-tune the EG3D using the original crop version of FFHQ. We use ShapeNet-Car [13] (128×128) to further demonstrate the effectiveness of our method.

Metrics. In Tables 1 and 2, we use the masked LPIPS (LPIPS_m) [98] to evaluate the faithfulness to the reference object. It needs a reference image to compute the score, and we used aligned reference images as pseudo-ground-truth images in both experiments: without and with 3D-aware alignment. Additionally, we always apply the alignment to our method in Tables 1 and 2.

Hyperparameters. In the 3D-aware blending, we optimize the latent code $\mathbf{w}_{\text{edit}} \in \mathbb{R}^{14 \times 512}$ of the $\mathcal{W}+$ space for 200 iterations. The initial value of $\mathbf{w}_{\text{edit}}$ is the latent code of the original image $\mathbf{w}_{\text{ori}}$. Adam [51] optimizer is used with 0.02 learning rate, $\beta_1 = 0.9$, and $\beta_2 = 0.999$. We reformulate Eqn. 5 to specify the hyperparameters as follows:

$$
\begin{aligned}
\mathcal{L}_{\text{image}} = & L_1((\mathbf{1} - \mathbf{m}) \circ \text{I}_{\text{edit}}, (\mathbf{1} - \mathbf{m}) \circ \text{I}_{\text{ori}}) \\
& + \lambda_1 \mathcal{L}_{\text{LPIPS}}((\mathbf{1} - \mathbf{m}) \circ \text{I}_{\text{edit}}, (\mathbf{1} - \mathbf{m}) \circ \text{I}_{\text{ori}}) \\
& + \lambda_2 \lambda_m \mathcal{L}_{\text{LPIPS}}(\mathbf{m} \circ \text{I}_{\text{edit}}, \mathbf{m} \circ \text{I}_{\text{ref}}),
\end{aligned}
\tag{8}
$$

where $\lambda_1 = 1$, $\lambda_2 = 0.5$ for AFHQ, $\lambda_2 = 0.1$ for FFHQ except hair ($\lambda_2 = 0.3$). $\lambda_m = \frac{3 \cdot H \cdot W}{\|\mathbf{m}\|_0}$ is a weighting parameter to give a high weight for the small target blending region $\mathbf{m}$; H and W denotes the height and width of the image, $\mathbf{m}$ is a binary mask $\mathbf{m} \in \{0, 1\}^{3 \times H \times W}$, and $||\cdot||_0$ is the L_0 norm

---

[1]https://github.com/PDillis/stylegan3-fun
[2]https://github.com/NVlabs/stylegan2-ada-pytorch

[3]https://github.com/yandex-research/ddpm-segmentation

that counts the total number of non-zero elements. Eqn. 6 is reformulated as follows:

$$\mathcal{L}_{\text{density}} = \lambda_m \sum_{\boldsymbol{r} \in \mathcal{R}_{\text{ref}}} \sum_{\boldsymbol{x} \in \boldsymbol{r}} L_1(G_\sigma(\mathbf{w}_{\text{edit}}; \boldsymbol{x}), G_\sigma(\mathbf{w}_{\text{ref}}; \boldsymbol{x}))$$
$$+ \sum_{\boldsymbol{r} \in \mathcal{R}_{\text{ori}}} \sum_{\boldsymbol{x} \in \boldsymbol{r}} L_1(G_\sigma(\mathbf{w}_{\text{edit}}; \boldsymbol{x}), G_\sigma(\mathbf{w}_{\text{ori}}; \boldsymbol{x})). \tag{9}$$

The results of L_1 loss in the image- and density-blending are normalized by the number of elements. We set λ in Eqn. 7 to 10.

B. Inversion details

We train our encoder to predict the camera pose of an image. It shares a similar structure with the EG3D discriminator [11] except without minibatch discrimination [74] and the number of input and output channels. As directly predicting the camera extrinsics $\in \mathbb{R}^{4 \times 4}$ is not easy, we convert the extrinsics to Euler angles $\in \mathbb{R}^3$; EG3D samples camera poses in the surface of a sphere. During inference, we transform it back to the camera extrinsics after obtaining the Euler angles from the encoder, which produces a more accurate pose estimation. Let the camera pose of the input image be $\mathbf{c}$.

We adopt Pivotal Tuning Inversion (PTI) [72] as our inversion method. In the first stage, we optimize the latent code $\mathbf{w} \in \mathcal{W}$ using the reconstruction loss $\mathcal{L}_{\text{rec}}$ as follows:

$$\mathcal{L}_{\text{rec}} = L_1(\mathbf{I}, G_{\text{RGB}}(\mathbf{w}, \mathbf{c})) + \mathcal{L}_{\text{LPIPS}}(\mathbf{I}, G_{\text{RGB}}(\mathbf{w}, \mathbf{c})), \tag{10}$$

where I is an input image and G_{RGB} is an image rendering function based on the generative NeRF G. L_1 is an L1 loss and $\mathcal{L}_{\text{LPIPS}}$ is a learned perceptual image patch similarity (LPIPS) [98] loss. We optimize the latent code $\mathbf{w}$ for 300 iterations.

In the second stage, we fine-tune the generative NeRF G using the same reconstruction loss $\mathcal{L}_{\text{rec}}$ and an additional regularization loss $\mathcal{L}_{\text{reg}}$ as follows:

$$\mathcal{L}_{\text{reg}} = L_1(G^f_{\text{RGB}}(\mathbf{w}_s, \mathbf{c}), G_{\text{RGB}}(\mathbf{w}_s, \mathbf{c}))$$
$$+ \mathcal{L}_{\text{LPIPS}}(G^f_{\text{RGB}}(\mathbf{w}_s, \mathbf{c}), G_{\text{RGB}}(\mathbf{w}_s, \mathbf{c})), \tag{11}$$

where G^f_{RGB} represents the freeze version of G_{RGB}, and $\mathbf{w}_s$ is a randomly sampled latent code followed by linear interpolation with $\mathbf{w}$. The interpolation parameter is also randomly sampled in $[0, 1]$. The final loss function for optimizing G is as follows:

$$\mathcal{L} = \mathcal{L}_{\text{rec}} + \lambda_{reg} \mathcal{L}_{\text{reg}}, \tag{12}$$

where $\lambda_{reg} = 0.1$ and we optimize the G for 100 iterations.

Algorithm 1 Iterative Closest Point (ICP)

Input: Point cloud of the reference object P_{ref}, Point cloud of the original object P_{ori}, difference threshold τ, maximum number of iterations K

1: **for** $k \leftarrow 1$ to K **do**
2:     **for** 3D point p_{ori} in P_{ori} **do**
3:         $p'_{\text{ref}} \leftarrow$ nearest point(p_{ori}, P_{ref})
4:     **end for**
5:     $P'_{\text{ref}} \leftarrow$ Point cloud of p'_{ref}.
6:     $CM_{\text{ori}} \in \mathbb{R}^3 \leftarrow$ center of mass in P_{ori}
7:     $CM_{\text{ref}} \in \mathbb{R}^3 \leftarrow$ center of mass in P'_{ref}
8:     $s_{\text{ori}} \in \mathbb{R} \leftarrow \frac{1}{\# \ of \ P_{\text{ori}}} \sum_{P_{\text{ori}}} L_2(p_{\text{ori}}, CM_{\text{ori}})$ ▷ scale of P_{ori}
9:     $s_{\text{ref}} \in \mathbb{R} \leftarrow \frac{1}{\# \ of \ P'_{\text{ref}}} \sum_{P'_{\text{ref}}} L_2(p'_{\text{ref}}, CM_{\text{ref}})$ ▷ scale of P'_{ref}
10:   Scale $s = \frac{s_{\text{ori}}}{s_{\text{ref}}}$
11:   Translation $\mathbf{t} = CM_{\text{ori}} - s * CM_{\text{ref}}$
12:   3D transformation matrix $\mathbf{W} = \begin{pmatrix} s & 0 & 0 & t_x \\ 0 & s & 0 & t_y \\ 0 & 0 & s & t_z \\ 0 & 0 & 0 & 1 \end{pmatrix}$
13:   $P_{\text{ref}} \leftarrow$ Transform(P_{ref}, $\mathbf{W}$)
14:   **if** $\sum_{P_{\text{ori}}, P'_{\text{ref}}} L_2(p_{\text{ori}}, p'_{\text{ref}}) < \tau$ **then**
15:     break
16:   **end if**
17: **end for**
18: **Return** $\mathbf{W}$

Runtime. As described above, our inversion method consists of two-stage optimization. For a single image, the first stage (latent code) takes 23.6s, and the second stage (generative NeRF) takes 20.4s. We test the runtime on a single A100 GPU.

C. Local alignment

Iterative Closest Point (ICP) [4, 19] is an algorithm to minimize the difference between two 3D point clouds. It is an iterative optimization process until we meet the threshold τ of difference or the maximum number of iterations $K = 20$. Algorithm 1 shows the pseudo-code of ICP. Please note that we do not use rotation in ICP as we align the rotation in *global alignment*, and refer to the exact details of ICP in our code.

3D transformation in the NeRF space. $\mathbf{W}$ is the 3D transformation matrix computed by the ICP algorithm. It transforms the point cloud of the blending region in the reference, aligning with the point cloud of the blending region in the original. A Neural Radiance Field learns a mapping function f that outputs density σ and radiance $\mathbf{c}_{\text{RGB}}$ for a given 3D point $\boldsymbol{x} \in \mathbb{R}^3$; $f(\boldsymbol{x}) = (\sigma, \mathbf{c}_{\text{RGB}})$. 3D points are sampled along a ray, which depends on the camera pose. Intuitively speaking, consider the matrix $\mathbf{W}$ as a tool for reducing scales. We cannot reduce the space of NeRF because the mapping function f is fixed. Instead, we can sample points more widely to reduce the scale relatively. Renewed
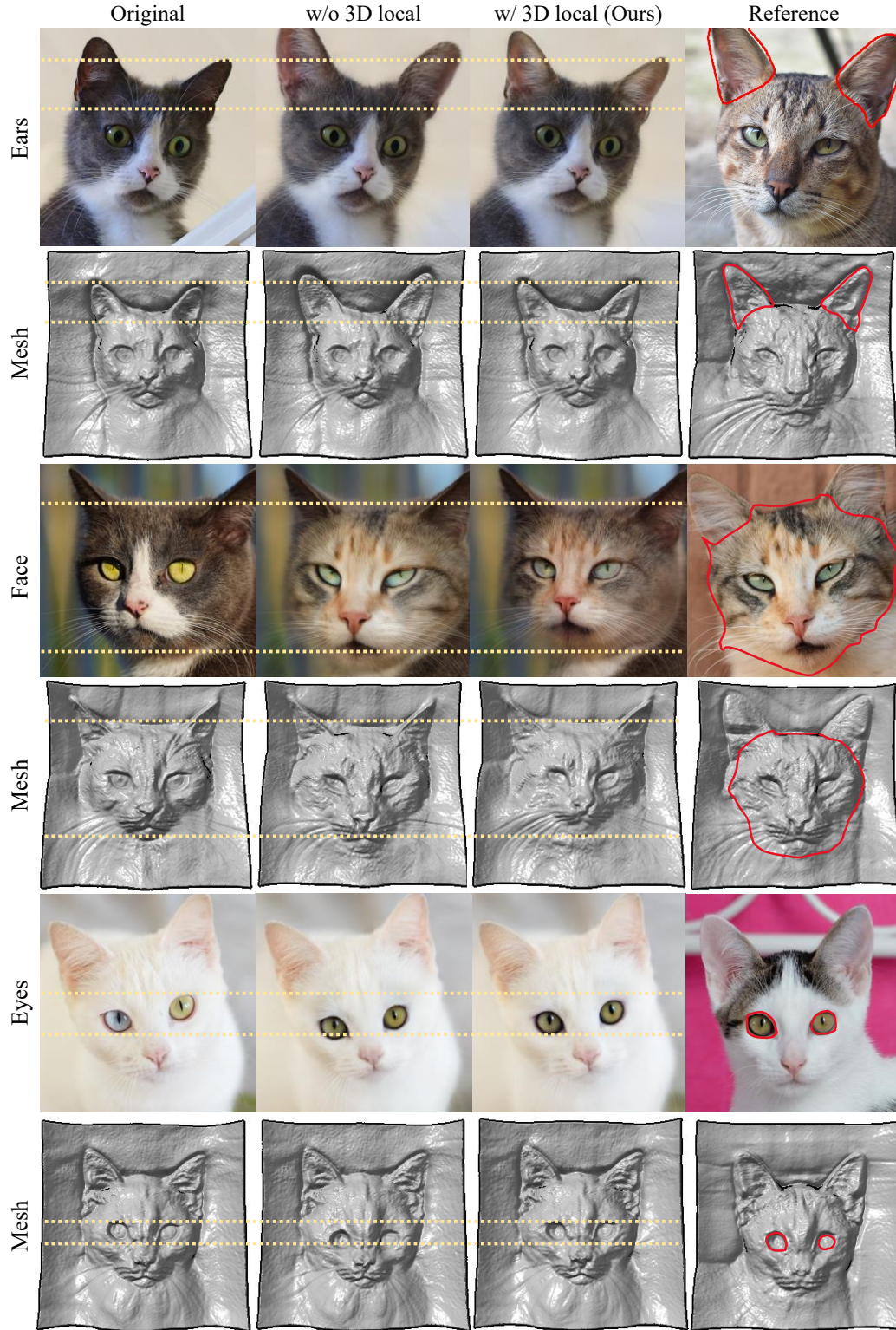
Figure 10. Ablation study of our 3D local alignment method in Appendix C. The leftmost and rightmost columns denote the original and reference images, respectively. Images in even rows are meshes corresponding to odd rows. Red lines denote the target blending mask, and yellow dotted lines are guidelines to be aware of alignment easily. Our 3D local alignment method (3rd column) shows more realistic blending results than those without local alignment (2nd column).
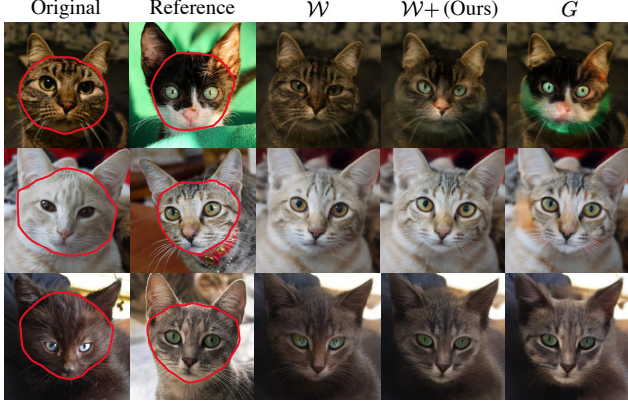
Figure 11. Blending comparison among the optimization spaces in Appendix D. The first and second columns denote original and reference images, respectively. The blending results of $\mathcal{W}$ space (3rd column) show realistic but less faithful to the reference images; see the details of eyes. The blending results of G space (rightmost column) show faithful but less realistic results. $\mathcal{W}+$ space (4th column) shows favorable results in both realism and faithfulness.

Method	Ours		Ours + Poisson Blending	
	w/o	w/ align	w/o	w/ align
Poisson [70]	79.9%	59.9%	80.9% (+1.0)	67.5% (+7.6)
StyleMap [47]	72.3%	62.0%	75.4% (+3.1)	66.3% (+4.3)
SDEdit [61]	61.0%	55.7%	61.1% (+0.1)	50.2% (-5.5)

Table 4. User study about the realism of the blended images in CelebA-HQ. Experimental settings are the same as Table 3. Ours and ours with Poisson blending outperform all baselines even if we improve the baselines using our 3D-aware alignment. Poisson blending further enhances the realism score of our method as shown in green numbers. Please refer to Appendix E and G.

Method	Ours		Ours + Poisson Blending	
	w/o	w/ align	w/o	w/ align
Poisson [70]	91.2%	76.2%	87.6% (-3.6)	82.8% (+6.6)
StyleMap [47]	91.0%	82.3%	91.6% (+0.6)	83.6% (+1.3)

Table 5. User study about the realism of the blended images in AFHQv2-Cat. All details are the same as in Table 4.

density σ' and radiance $\mathbf{c}'_{\text{RGB}}$ can be computed using the inverse matrix of $\mathbf{W}$ as follows $f(\mathbf{W}^{-1}\boldsymbol{x}) = (\sigma', \mathbf{c}'_{\text{RGB}})$.

Ablation study for local alignment. We demonstrate the effectiveness of our 3D-aware alignment and significant improvements in all baselines in Tables 1, 2 and 3. Especially, *local alignment* in our alignment method shows efficacy in Figures 6 and 10. We further examine local alignment by conducting a user study. In **60.3**% of cases, users prefer our blending results with local alignment compared to those without alignment. Please see the details of the user study in Appendix G.

Runtime. *Global alignment* takes 1.7s, and *local alignment* takes 4.2s, 4.6s, 5.9s for ears, eyes, face in AFHQv2-Cat [20]. The larger blending part takes more time to align. Our local alignment implementation uses the `Trimesh`[4] library, which provides pre-defined functions for triangular meshes on the CPU. Implementing it with GPU-based libraries can further reduce alignment runtime.

D. Details of 3D-aware Blending

Choice for the optimization space. In our blending method, we optimize the latent code $\mathbf{w} \in R^{14 \times 512}$ in the $\mathcal{W}+$ space. There are other options for optimization, such as $\mathcal{W}$ space or generator G. Figure 11 shows the comparison among optimization spaces in 3D-aware blending. $\mathcal{W}$ space shows realistic blending results but lacks faithfulness to the reference object. The blended image can not capture

---
[4]https://trimsh.org/trimesh.html

the green eyes of the reference object, as shown in the first row of Figure 11. Optimizing G shows faithfulness to the reference object but lacks realism. The boundaries of results look particularly odd. $\mathcal{W}+$ space shows great results in both realism and faithfulness, our method adopts to optimize the $\mathcal{W}+$ latent space.

Masks used in alignment and blending. At first, we apply *global alignment* to rotate the reference to match the pose of the original. A user selects a mask $\mathbf{m}$ for the target blending region of the original image. The user selects another mask $\mathbf{m}'$ for the target blending region of the reference image, or it can be derived automatically using previous works [38, 103]. We blend images using the union of the masks, $\mathbf{m} \cup \mathbf{m}'$, and we redefine $\mathbf{m}$ as this union in Figure 5. Before blending in AFHQ, $\mathbf{m}$ and $\mathbf{m}'$ are used for *local alignment* to align target regions of two images, as shown in Figure 4. After local alignment, the target reference mask $\mathbf{m}'$ is also modified.

Runtime comparison with baselines. Poisson blending [70], StyleMapGAN [47], Latent Composition [10] take less than a second to blend images at 1024×1024 resolution, as they use low-level visual cues [70] or encoders [10, 47]. SDEdit [61] and StyleGAN3 [42] both require an iterative process. SDEdit takes 29.5s for 500 iterations (face and hair) and 20.0s for 300 iterations (nose, eyes, lip) at 256^2 image resolution. StyleGAN3 takes 69.8s for 512^2 and 106.5s for 1024^2 resolution. Our method takes 26.9s at 512^2 and we can further reduce the time to 12.1s by combining ours with Poisson blending (Appendix E). All runtimes are measured in the same device with a single A100 GPU. Ours is faster
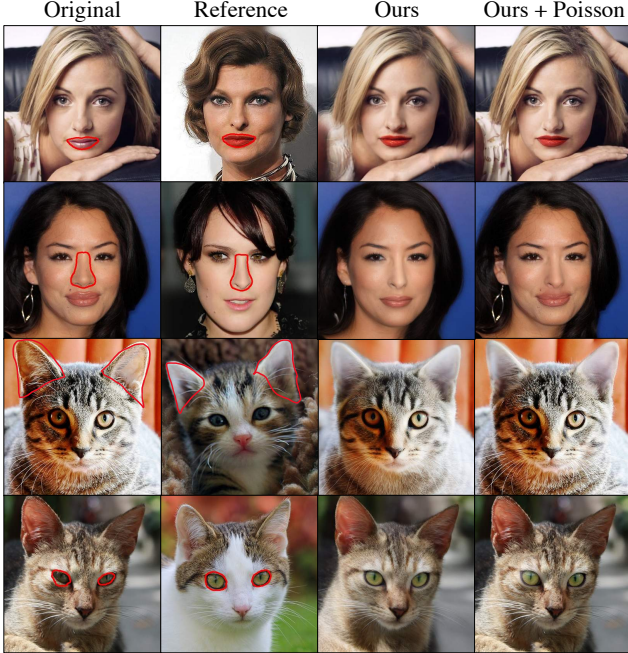
Figure 12. Qualitatve comparison between ours and ours with Poisson blending [70] in Appendix E. Ours shows satisfactory blending results but a lack of preservation in details. In the first row, hands can not be preserved. Earrings are missing in ours as shown in the second row. High-frequency details such as hair and fur are worse in ours than in combination with Poisson blending.
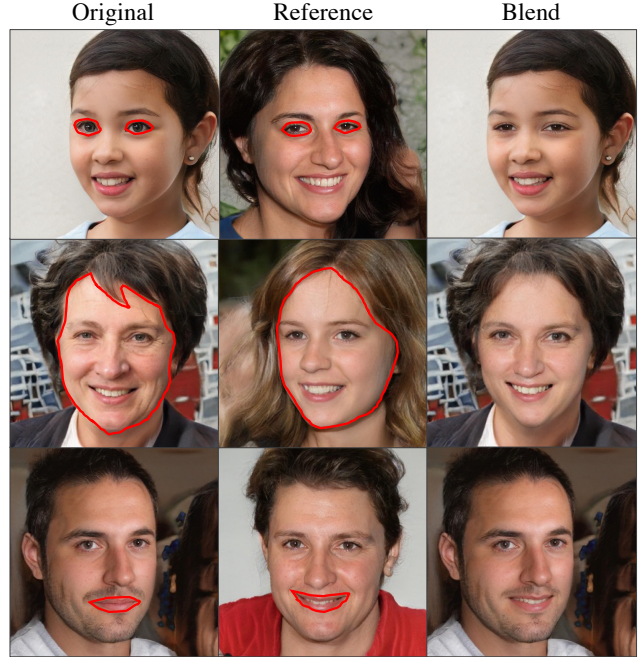

Figure 13. Our 3D-aware blending results of StyleSDF [66] in Appendix F. The third column is blending results in 1024^2 resolution. Our method can be applied to the SDF-based 3D-aware generator beyond NeRFs.

than other optimization-based baselines but slower than the encoder-based methods. In the future, we can directly train an encoder using our image- and density-blending losses to reduce the runtime.

E. Ours with Poisson Blending

Ablation study with an extra user study. In Tables 1 and 2, we report the combination of our method and Poisson blending. It shows Poisson blending further enhances the performance of our method in all automatic metrics: KID, mL_2, and LPIPS$_m$. In the realism score of human perception, ours with Poisson Blending outperforms other baselines, as shown in Table 3.

We conduct an extra user study to measure how far Poisson blending affects the realism score of human perception in our blending method. Tables 4 and 5 show the comparison with baselines in photorealism, and we use exactly the same experimental setting and test images as Table 3. Combining our 3D-aware blending method with Poisson blending shows improvement in most cases. Please note that our method solely outperforms other baselines without Poisson blending. Additional qualitative comparison can be seen in Figure 12. We apply Poisson blending to our method in Figures 1, 8, 22 and 23 and Tables 1 and 2.

Implementation details. We perform Poisson blending between the original image and the blended image generated by our 3D-aware blending method. Our blending method is modified in two ways. 1) In the initial blending stage, we only preserve the area around the border of the mask instead of all parts of the original image, as we can directly use the original image in the Poisson blending stage. This makes blending easier and reduces the number of iterations from 200 to 100, resulting in improved faithfulness scores (mL_2 and LPIPS$_m$) as shown in Tables 1 and 2. 2) Instead of using the latent code of the original image $\mathbf{w}_{ori}$ as the initial value of $\mathbf{w}_{edit}$, we use the latent code of the reference image $\mathbf{w}_{ref}$. This allows us to instantly reflect the identity of the reference image and only optimize $\mathbf{w}_{edit}$ to reconstruct a small region of the original image.

F. 3D-aware blending in StyleSDF

StyleSDF [66] generates high-fidelity view-consistent images in 1024×1024 resolution. The main difference between StyleSDF and EG3D [11] is StyleSDF uses Signed Distance Fields (SDF) as 3D representation. Additionally, StyleSDF does not require camera pose labels to train the generator, unlike EG3D. In our 3D-aware blending method, we can use the SDF value d as a 3D signal, similar to the density σ in EG3D. If we assume a non-hollow surface, the SDF value
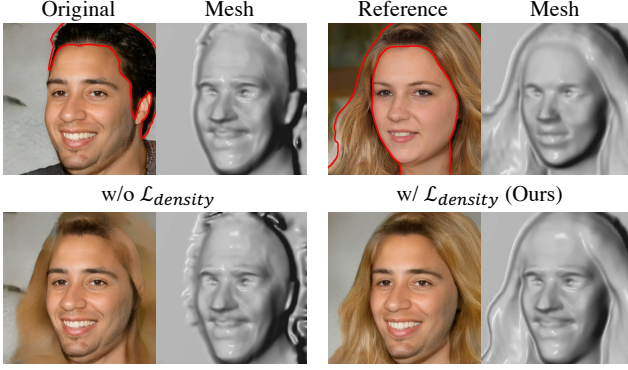
Figure 14. Ablation study of density-blending loss $\mathcal{L}_{\text{density}}$ in StyleSDF (Appendix F). This experiment uses SDF instead of volume density σ. Without $\mathcal{L}_{\text{density}}$, the blending result shows a blurry image, and the corresponding mesh shows it can not reflect the geometry of the hair of the reference image. 3D signals such as density and SDF are key components in the 3D-aware blending method.
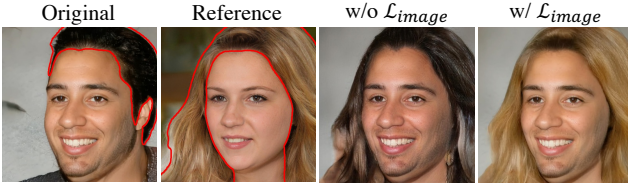

Figure 15. Ablation study of image-blending loss $\mathcal{L}_{\text{image}}$ in StyleSDF (Appendix F). We can control the degree to which the color of the reference object is reflected in the blended image, by adjusting the weight of the image-blending loss with respect to the reference image.

can be converted to the density σ as follows:

$$\sigma(\boldsymbol{x}) = \frac{1}{\alpha} \cdot \text{Sigmoid}(\frac{-d(\boldsymbol{x})}{\alpha}), \qquad (13)$$

where $\boldsymbol{x} \in \mathbb{R}^3$ is a 3D location and α is a learned parameter about the tightness of the density around the surface boundary. We use the same blending loss functions used in EG3D, except we replace the density σ with SDF d.

Here we demonstrate that our method can be applied to other 3D-aware generative models beyond EG3D. Figure 13 shows our 3D-aware blending results in StyleSDF using generated images. Figure 14 and Figure 15 show ablation studies of our blending loss terms: $\mathcal{L}_{\text{density}}$ and $\mathcal{L}_{\text{image}}$, respectively. The ablation studies show a similar tendency with EG3D experiments in the paper. Without density-blending loss, we can not blend highly structured objects like hair. If a user does not want to reflect the reference color, we remove or give a low weight to the image-blending loss on reference: λ_2 in Eqn. 5.

G. User study details

We conduct extensive user studies to show the effectiveness of our methods in the realism score of human perception on the Amazon Mechanical Turk (MTurk) platform. We refer to user study pipelines of SDEdit [61] and modify the template[5] from the previous work [97]. The instruction page is shown in Figure 19, and MTurk workers participate in surveys comparing the results of two methods, as shown in Figures 20 and 21.

Each evaluation set consists of 25 pairwise comparison questions, with an additional five questions used to detect deceptive workers. We only invite workers with a HIT Approval Rate greater than 98%. Each set takes approximately 2 to 3 minutes and offers a reward of $0.5.

Comparison with baselines are conducted in Tables 3, 4 and 5. Figure 20 shows the comparison page. There are two blending results: one for our method and the other for one of the baselines. The order of images is randomly shuffled, and a worker selects a more realistic image. In CelebA-HQ [41] and AFHQv2-Cat [20], we used 60 and 40 evaluation sets, respectively; CelebA-HQ for 1,500 and AFHQ for 1,000 pairwise comparisons.

Ablation study of 3D local alignment is conducted in Appendix C. The user study page is shown in Figure 21. Experimental settings are almost similar to previous studies. We show two blending results of our method with and without *local alignment*. Note that global alignment is used in both of the results. We used 20 evaluation sets in AFHQv2-Cat; 500 pairwise comparisons.

H. Failure cases

The initial process of our method is the inversion, and it affects the quality of our whole blending pipelines. In Figure 16, we show the failure cases of inversion in EG3D. If an input image is far from the average face generated from the mean latent code $\mathbf{w}_{\text{avg}}$, we can not obtain an acceptable inversion result. We also note the camera pose inferred by our encoder should not be overly inaccurate. At last, high-frequency details such as fine wrinkles are hard to be reconstructed.

Figure 17 shows another failure case of 3D-aware alignment in the Iterative Closest Point (ICP) algorithm [4, 19]. ICP is an approach to aligning the two point clouds: P_{ori} and P_{ref} for the original and reference objects, respectively. It iteratively minimizes the distance between each 3D point in P_{ori} and its nearest point in P_{ref}, but it may fall into the local extremum. P_{ref} shrinks to a point $\tilde{P}_{\text{ref}}$ as discussed in the previous work [87]. If a user gives improper masks or the target region of the mesh has indistinctive geometry, ICP fails occasionally. To mitigate this issue, we restrict the minimum and maximum scaling factor to $[0.75, 1.25]$. Improved versions
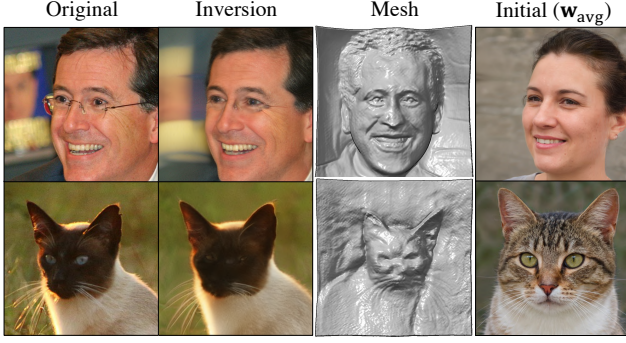
---

[5]https://github.com/phillipi/AMT_Real_vs_Fake

Figure 16. Failure cases of inversion in Appendix H. The first column and the second column denote the original images and inversion results, respectively. The third column is the mesh results of inversion. The rightmost column is the initial results of the inversion process. If an input image has a large variance in scale relative to the mean face or the estimated pose from the encoder is not valid, the inversion may sometimes fail. The first row shows a failure to reconstruct eyeglasses, and the second row shows a crushed face of a cat in the reconstructed image and mesh.

Figure 17. A failure case of the Iterative Closest Point (ICP) algorithm in Appendix H. If a user gives inappropriate masks or the target region of the mesh has indistinctive geometry, ICP may fail and generates a degraded aligned reference image. Masks are given as both eyes for the original image and the left eye for the reference image. The right figure shows the point cloud visualization. Red dots stand for the point cloud P_{ori} of both eyes of the original object. Light blue dots stand for the point cloud P_{ref} of the left eye of the reference object. Blue dots denote the transformed point cloud $\tilde{P}_{ref}$ of the reference after applying ICP. This visualization shows the failure of ICP.
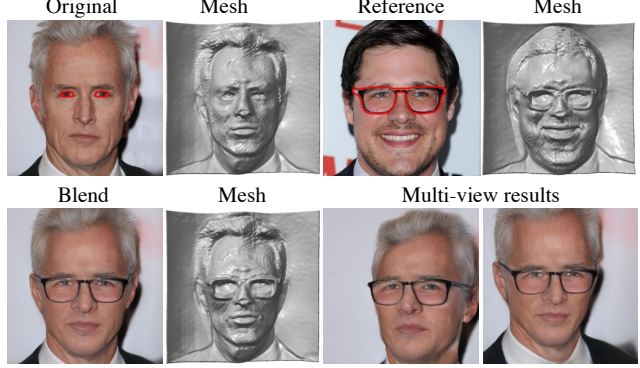

Figure 18. Blending highly structured parts such as eyeglasses. Our blending method can reflect the high-fidelity 3D shape of eyeglasses and generate multi-view consistent results.

I. Societal impact

The societal impact of image blending shares similar issues raised in the other generative models and view synthesis techniques [35]. For instance, a malicious user may use image blending to manipulate the expression and identity of a real person or create a scene that does not exist in real life. Most of the existing watermarking and visual forensics methods focus on 2D image content [92]. Adopting visual forensics methods for 3D-aware content seems to be an important future work.

J. Additional results

In this section, we show additional qualitative results of our 3D-aware blending. Figure 18 shows blending results of highly structured objects such as eyeglasses. Figures 22 and 23 show blending comparisons with baselines. Our results show outstanding blending results than other baselines. By virtue of NeRF, we can synthesize novel-view images. Figures 24–27 show multi-view consistent blending results. Please see our project page for the multi-view consistent blending videos.

of inversion [52] and point-set registration techniques [87] can boost our blending performance in the future.

About this HIT:

- **Please select carefully, there are some test examples to detect fake workers. If you just select one of the image randomly, you can not be approved.**

- It should take about 3 minutes; 5 seconds per each comparison. There is 30 comparisons.

- You will take part in an experiment involving visual perception. You'll see a series of pairs of images. In each pair, both of images are edited images using difference AI technology.

- **Your task is to determine which image looks more real.**

- **We only accept one hit per worker, do not do the survey twice. It will be rejected later.**

- **There are some unpleasant images, if you don't want to see them please turn back.**

Please accept HIT to start

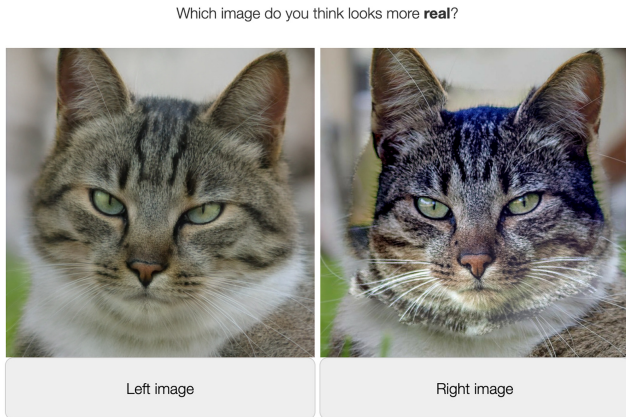Figure 19. An introduction page of user studies in Amazon Mechanical Turk (MTurk).

Figure 20. A comparison page between ours and baselines in MTurk.
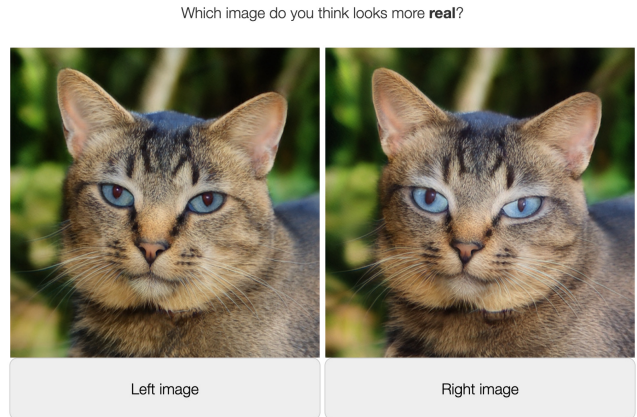

Figure 21. A comparison page of ablation study of our local alignment in MTurk.

Figure 22. Blending comparison with baselines in the CelebA-HQ test set. It shows supplementary comparison results of Table 1. LC and PB stand for Latent Composition [10] and Poisson Blending [70], respectively.

Figure 23. Blending comparison with baselines in the AFHQv2-Cat test set. It shows supplementary comparison results of Table 2.
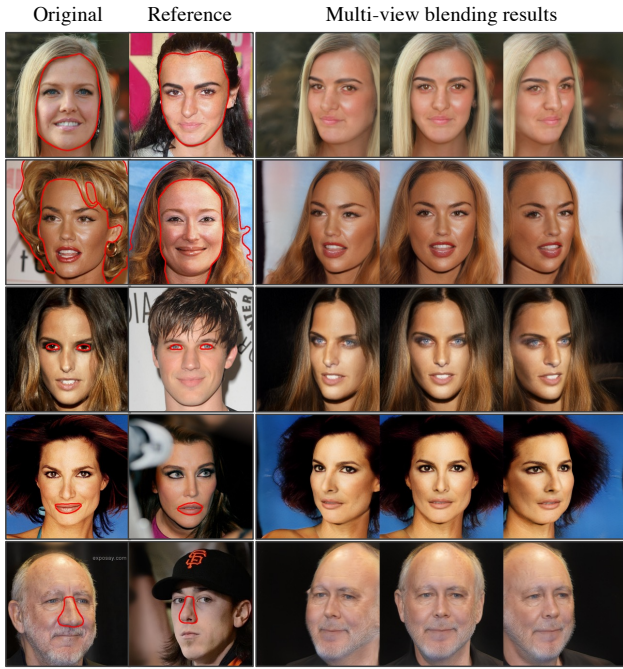
Figure 24. Multi-view blending results in CelebA-HQ using EG3D.
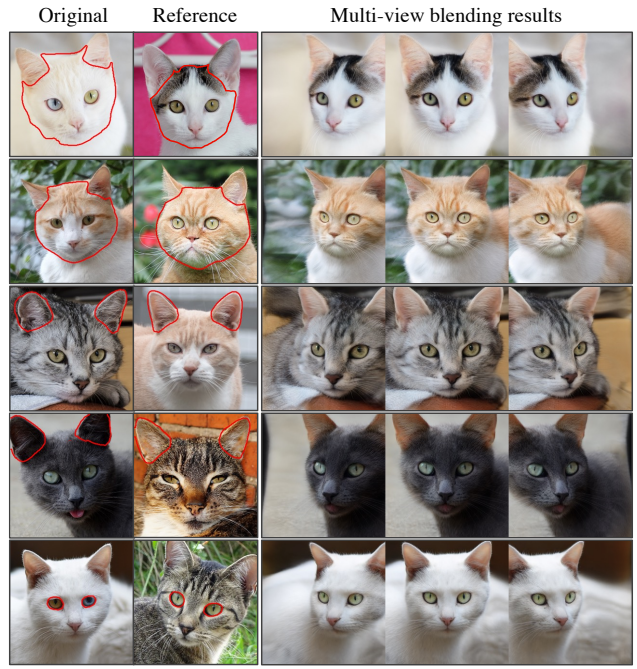

Figure 26. Multi-view blending results in AFHQv2-Cat using EG3D.

Figure 25. Multi-view blending results in ShapeNet-Car [13] using EG3D. The last two rows demonstrate that our method can achieve natural blending even when the sizes of the blending regions differ. Our 3D local alignment also performs well on the ShapeNet-Car dataset.
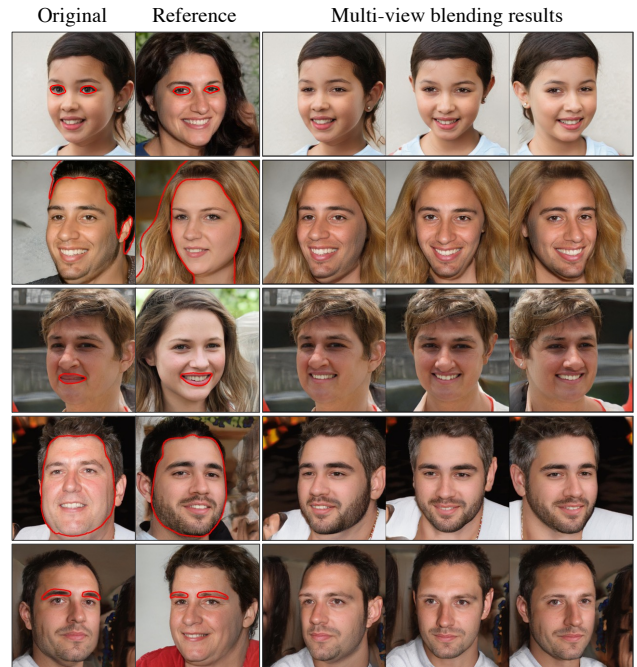

Figure 27. Multi-view blending results in generated images using FFHQ-pretrained StyleSDF [66].